Research papers

Improvement of evapotranspiration simulation in a physically based ecohydrological model for the groundwater–soil–plant–atmosphere continuum

Kun Zhang [a,e,*], Gaofeng Zhu [b,*], Ning Ma [c], Huiling Chen [b], Shasha Shang [d]

[a] Department of Mathematics, The University of Hong Kong, Hong Kong, China
[b] College of Earth and Environmental Sciences, Lanzhou University, Lanzhou, China
[c] Key Laboratory of Water Cycle and Related Land Surface Processes, Institute of Geographic Sciences and Natural Resources Research, Chinese Academy of Sciences, Beijing, China
[d] Tianjin Key Laboratory of Water Resources and Environment, Tianjin Normal University, Tianjin, China
[e] School of Biological Sciences, The University of Hong Kong, Hong Kong, China

ARTICLE INFO

ABSTRACT

Accurate quantification of terrestrial evapotranspiration (ET) is essential to understanding the interaction between land and atmosphere, as well as the feedback response of vegetation dynamics. In our previous work, a physically based ecohydrological model called the simple terrestrial hydrosphere (SiTH) model was developed to estimate ET and the other ET-related variables based on the groundwater–soil–plant–atmosphere continuum (GSPAC). However, the SiTH model (SiTHv1) still has some deficiencies in the model structure and parameters, which can result in potential uncertainty in the estimation of terrestrial ET. In this study, we aimed to address these limitations by developing a new version of the SiTH model (SiTHv2). The main modifications of the SiTHv2 model include: (1) the vegetation moisture constraint module is updated with vegetation optical depth observations; (2) the critical model parameters associated with root distribution are constrained using flux observations; (3) the soil module is extended to a three-layer module with 5 m of total depth; (4) an irrigation input water strategy is applied in the cropland areas; and (5) the latest ERA5-Land reanalysis data with a finer spatial resolution are used as the meteorological forcing data. The estimated ET of the SiTHv2 model was validated/compared at multiple scales (i.e., site/plot, basin, and global) with flux data, basin water balance data, and other mainstream global ET products, respectively. The results demonstrate that the SiTHv2 model performs better than the SiTHv1 model, with an improvement in the overall model root-mean-square error of 0.66 mm day^{-1} (plot scale) and 98.58 mm year^{-1} (basin scale), representing 27% and 22% improvements over the SiTHv1 model in the same circumstances, respectively. In addition, the performance of the SiTHv2 model ranks well when compared to the existing terrestrial ET models and products. The improvements to the SiTH model should allow improved estimation of terrestrial ET and provide support to potential studies in water transfer within the GSPAC.

1. Introduction

Terrestrial evapotranspiration (ET) is a crucial nexus that is tightly coupled with the global water cycle and energy balance (Oki and Kanae, 2006). About 65% of land precipitation is supplied by the terrestrial ET process (Ma et al., 2021; Dorigo et al., 2021), which concomitantly consumes more than 50% of the net solar radiation received by the land surface (Trenberth et al., 2009). In recent decades, much effort has been devoted to estimating large-scale terrestrial ET using ecohydrological models and remote sensing technology (Fisher et al., 2008; Jung et al., 2019; Ma et al., 2019; Martens et al., 2017;

Mu et al., 2011). Accurate estimation of terrestrial ET fluxes is a key goal of the ecohydrological community and benefits many scientific fields and practical applications, such as studies of the water/carbon cycle under the scenario of climate change (Frankenberg et al., 2011; Held and Soden, 2006; Ma and Zhang, 2022; Zhou et al., 2021), the detection of extreme events (Miralles et al., 2019; Teuling et al., 2010), and agricultural water management (Allen et al., 2011; Xu et al., 2020).

Despite the sustained advances in global ET modeling that have been achieved over the past few decades (Ma et al., 2021; Pan et al., 2020; Wang and Dickinson, 2012; Zhang et al., 2016), there is still a

---

need to characterize the ET processes in a more realistic and detailed manner, thereby improving ET estimation overall. Among the different models, the simple terrestrial hydrosphere (SiTH) model (Zhu et al., 2019) was proposed to simulate the terrestrial ET process within the context of the groundwater–soil–plant–atmosphere continuum (GSPAC) (Scanlon and Kustas, 2012). In brief, the SiTH model depicts an integrated water path between vegetation canopy and groundwater, and is one of the few global ET models that considers the effect of groundwater in the root zone in regulating soil moisture conditions (Fan, 2015), which can mitigate the impact of drought in areas with a shallow groundwater depth (Gou and Miller, 2014). Another significant feature in the SiTH model is the ability to adjust the allocation of potential plant transpiration to different soil layers, combined with root distribution and soil water conditions. Chen et al. (2022) reported that the SiTH model performed well compared to other process-based global ET models for estimating the different ET components, such as soil evaporation, plant transpiration, and canopy intercepted evaporation, across various plant functional types (PFTs).

Nevertheless, there are still some limitations to the SiTH model. Firstly, the previous SiTH model (SiTHv1) did not take the plant moisture status into account, which can lead to potential over-estimation when estimating ET, due to the weak moisture constraint, especially in forest ecosystems (Chen et al., 2020). Fortunately, microwave-based remote sensing technology has the capacity to monitor plant water content via the indicator of vegetation optical depth (VOD), which is based on the attenuation of passive and active microwave observations yielded by vegetation (Jackson and Schmugge, 1991; Moesinger et al., 2020; Owe et al., 2008). In this present study, we attempted to incorporate VOD into the SiTH model, in order to better characterize water stress for vegetation growth. Secondly, the SiTHv1 model regards precipitation to be the only source of input water applied to cropland. However, around 40% of the global cropland is made up of irrigated land, which contributes 60% of the global food supply and concurrently consumes approximately 70% of the global freshwater withdrawal from the surface/subsurface water system (Foley et al., 2011; Siebert and Döll, 2010). Thus, an irrigation water use (IWU) scheme is introduced in the updated SiTH model, based on the authors' prior work on satellite-based global IWU estimation (Zhang et al., 2022). Thirdly, plant transpiration generally dominates the total ET (Jasechko et al., 2013), and is typically governed by the soil water availability and the root distribution, which are given as empirical parameters in the SiTHv1 model. Hence, in the updated SiTH model, the soil module is changed to three layers, and the total depth is extended to 5 m, allowing the model to cover the majority of the global root depths for the various PFTs (Canadell et al., 1996; Maeght et al., 2013). In addition, the fundamental parameters related to plant root distribution are optimized using global flux observations. Lastly, the meteorological forcing data are replaced by the fifth generation of European reanalysis data (ERA5-Land, hereafter referred to as ERA5L) to run this updated SiTH model at a global scale. The ERA5L product is a state-of-the-art reanalysis product developed by the European Centre for Medium-Range Weather Forecasts (ECMWF), which offers spatio-temporally continuous data at a finer spatial resolution (0.1° globally).

The focus of this study was to present an updated version of the SiTH model (SiTHv2), which includes: (1) modification of the model structure with new features; (2) multi-scale validation of the SiTHv2 model using eddy covariance flux measurements and basin-scale water balance estimates; and (3) a global comparison of the SiTH-based ET estimates with other mainstream global ET products, in terms of magnitude and trend changes. In addition, we produced a global daily ET dataset with a spatial resolution of 0.1°, based on the newly modified SiTHv2 model.

2. Methods

2.1. Model development

In the previous version (Zhu et al., 2019), the SiTH model was proposed for continuous modeling of the water path in the GSPAC (Fig. 1). The total ET estimated from the SiTH model is the sum of the bare soil evaporation (E_s), plant transpiration (T_r), and canopy intercepted evaporation (E_i). It is worth noting that the water stress on E_s is constrained by the first soil layer, while T_r is constrained by both the multiple soil layers and the groundwater (if the groundwater can recharge to the root zone).

$$ET = E_i + E_s + T_r \tag{1}$$

$$E_i = f_{wet} \cdot \alpha \cdot \frac{\Delta}{\Delta + \gamma} \cdot \frac{R_{nc}}{\lambda} \tag{2}$$

$$E_s = f_{sm} \cdot \alpha \cdot \frac{\Delta}{\Delta + \gamma} \cdot \frac{R_{ns} - G}{\lambda} \tag{3}$$

$$T_r = \left(1 - f_{wet}\right) \cdot f_v \cdot f_t \cdot \left[\sum_{i=1}^{n} \left(f_{smv,i} \cdot T_{ps,i}\right) + \sum_{i=1}^{n} \left(T_{pg,i}\right) \right] \tag{4}$$

where α is the Priestly–Taylor coefficient, which is set to 1.26; Δ is the slope of the saturated vapor pressure curve (kPa °C^{-1}); γ is the psychrometric constant, which is set to 0.066 (kPa °C^{-1}); λ is the latent heat of evaporation (MJ kg^{-1}); G is the soil heat flux (W m^{-2}); and n is the total number of soil layers ($n = 3$) in the SiTHv2 model. R_{ns} and R_{nc} are the net radiation (R_n) allocated to the bare soil and canopy surface (W m^{-2}), respectively, which are complementary ($R_n = R_{nc} + R_{ns}$). Their calculation is conducted according to $R_{ns} = R_n \exp(-k_{R_n} \text{LAI})$ (Beer, 1852; Fisher et al., 2008), where k_{R_n} is the extinction coefficient, which is set to 0.6 (Impens and Lemeur, 1969). $T_{ps,i}$ and $T_{pg,i}$ are the potential transpiration from the unsaturated ith layer and saturated ith layer, which can be derived from the total potential ET by considering the vertical distributions of plant roots and the depth of the groundwater table (see details in Zhu et al., 2019). The f-functions are the different constraints on the potential evaporation and transpiration, where f_{wet} is the relative surface wetness, f_v is the vegetation water stress on the plant transpiration, f_{sm} is the soil moisture constraint on the bare soil evaporation, $f_{smv,i}$ is the soil moisture constraint on the plant transpiration at the ith soil layer, and f_t is the temperature constraint on plant growth. Among the different constraints, f_{wet}, f_t, and f_{sm} can be calculated as:

$$f_{wet} = \min \left\{ \chi \cdot \frac{S_c}{T_p}, 1 \right\} \tag{5}$$

$$f_t = \exp \left[-\left(\frac{T_a - T_{opt}}{T_{opt}} \right)^2 \right] \tag{6}$$

$$f_{sm} = \begin{cases} 0, & if\ \theta_i \leq \theta_{wp} \\ \frac{\theta_i - \theta_{wp}}{\theta_{fc} - \theta_{wp}}, & if\ \theta_{wp} < \theta_i < \theta_{fc} \\ 1, & if\ \theta_i \geq \theta_{fc} \end{cases} \tag{7}$$

where T_p is the potential transpiration rate of the canopy; χ is the fractional interception occurring during daytime, which is set to 0.7; S_c is the water storage capacity of the canopy, which is defined as the product of precipitation and the leaf area index (LAI); T_a is the air temperature (°C); T_{opt} is the optimum plant growth temperature (°C), which can be defined as the air temperature when the product of LAI, R_n, and T_a is the highest during the growing season; θ_{fc} is the soil field capacity; θ_{wp} is the soil moisture at the wilting point; and θ_i is the actual soil moisture at the ith soil layer (the first soil layer is only considered for the soil evaporation).

Notably, the critical threshold (θ_c) for soil moisture in the SiTH model is the multifactor-influenced parameter representing the state at which soil moisture begins to have a constraint on plant transpiration, which dominates the transpiration changes in transitional
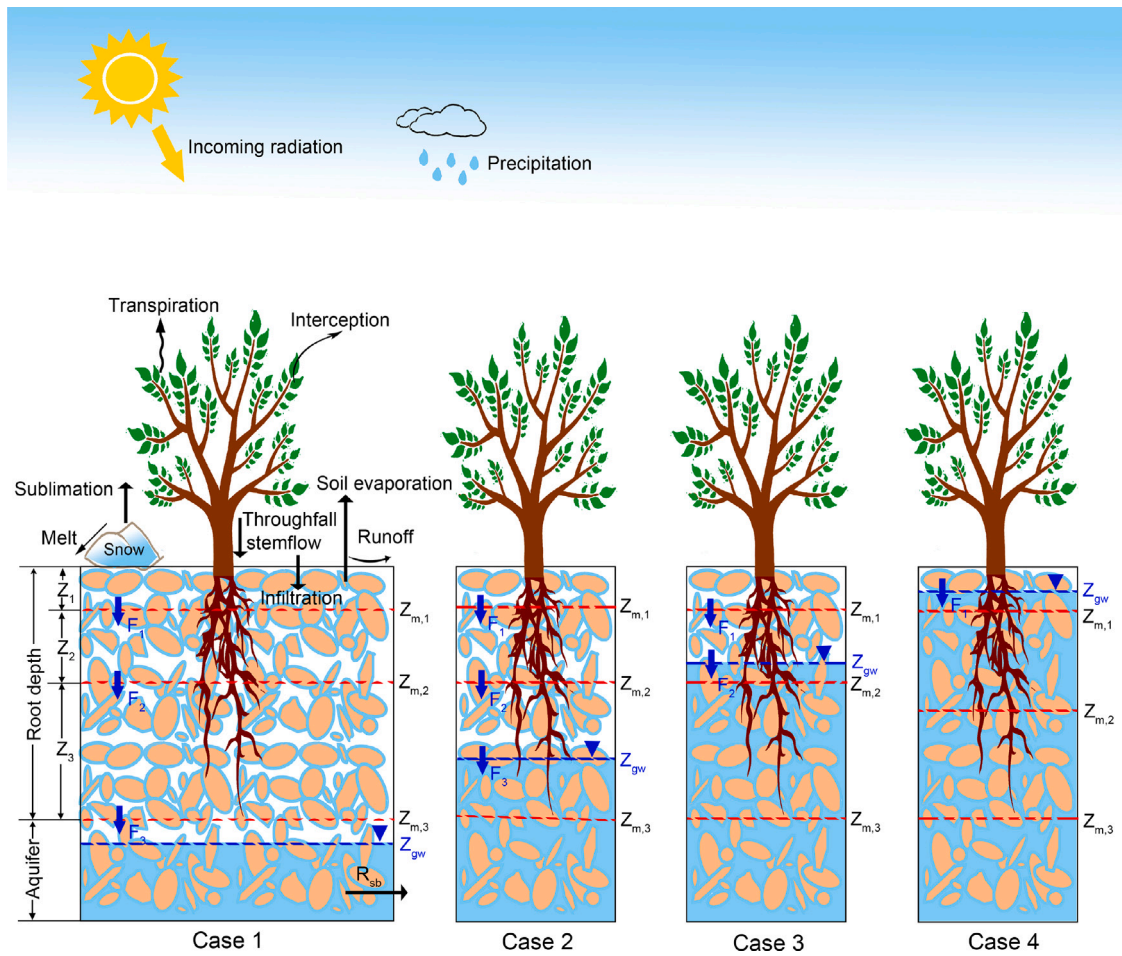
Fig. 1. Schematic representation of the hydrologic process in the SiTH model. Case 1 represents the groundwater table being below the root zone; Case 2 represents the groundwater table being within the third soil layer; Case 3 and Case 4 represent the groundwater table being within the second and first soil layer, respectively. The arrows indicate the water flux direction.

regimes (Schwingshackl et al., 2017; Wang et al., 2022). Instead of only considering the soil type as a static constant, as in the SiTHv1 model, we revised the expression of (θ_c) in the SiTHv2 model to reflect the characteristic water stress sensitivities for different PFTs, according to Purdy et al. (2018) and van Diepen et al. (1989):

$$\theta_c = (1 - p)\left(\theta_{fc} - \theta_{wp}^h\right) + \theta_{wp}^h \tag{8}$$

$$p = \frac{1}{1 + ET_p} - \frac{b}{1 + H_c} \tag{9}$$

$$\theta_{wp}^h = \theta_{wp}/k \tag{10}$$

where k is a sensitivity index for the soil water content, which can be determined as the square root of the canopy height (H_c); θ_{wp}^h is the adjusted wilting point for soil moisture when considering H_c; p is a parameter for regulating θ_c between θ_{fc} and θ_{wp}^h, which can be determined by the potential ET (ET_p) and H_c; and b denotes the weight of H_c on θ_c, which is set to 0.1. Thus, the soil moisture constraint function for plant transpiration at the ith layer ($f_{smv,i}$) can be expressed as follows (Martens et al., 2017):

$$f_{smv,i} = \begin{cases} 0, & if \ \theta_i \leq \theta_{wp}^h \\ 1 - \left(\frac{\theta_c - \theta_i}{\theta_c - \theta_{wp}^h}\right)^k, & if \ \theta_{wp}^h \leq \theta_i \leq \theta_c \\ 1, & if \ \theta_i \geq \theta_c \end{cases} \tag{11}$$

Fig. 2 illustrates a concept map of the response of f_{smv} to the gradients of soil water content under different biotic and abiotic conditions (i.e., H_c and ET_p). Clearly, the soil water constraint scheme for

transpiration adopted by the SiTHv1 model (yellow line) is simplified as a logarithmic function to soil water content, where f_{smv} decreases rapidly from the critical point of soil moisture. However, the new constraint scheme in the SiTHv2 model provides a wide range of f_{smv} to a specific value of θ, based on different H_c and ET_p values, which is more in line with the real situation of vegetation (e.g., forest or grassland), where the sensitivity to soil moisture varies over different plant heights with specific environmental conditions.

Furthermore, the plant transpiration estimated by the SiTHv1 model is not constrained by the moisture content of the vegetation status. To address this issue, we added a plant water stress module based on the microwave remotely sensed VOD. It has been well documented that VOD is closely related to the density, type, and water content of vegetation, and is advantageous for monitoring tropical forest without the effect of cloud (Liu et al., 2011, 2015). In the SiTHv2 model, the vegetation water stress (f_v) is described as follows:

$$f_v = \sqrt{\frac{VOD}{VOD_{max}}} \tag{12}$$

where VOD_{max} is the maximum value for the annual VOD time series at each pixel.

In addition, to better estimate the ET from irrigated cropland, we introduced an IWU scheme into the SiTHv2 model. The irrigation signal can be first identified by the discrepancy between the dynamic changes of soil moisture and precipitation in the irrigated area. The volume of the IWU can then be derived based on the balanced relationship of the soil water variations (Zhang et al., 2022). The IWU estimates
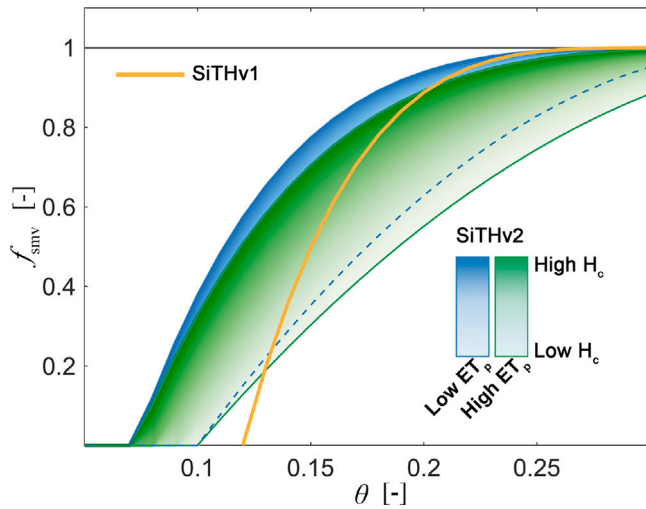
Fig. 2. Schematic diagram of the soil water constraint on transpiration in SiTHv2 by considering the different vegetation height and environmental conditions. (For interpretation of the references to color in this figure legend, the reader is referred to the web version of this article.)

were obtained from the authors' prior work, and were integrated into the SiTH model as exceptional input water applied to the cropland. Specifically, the original monthly IWU estimates for global irrigated land were simply dispersed to the start, the middle, and the end of a month by weighting of the distribution density of the LAI. This can be expected to enhance the water supply in the irrigated regions during the growing season, especially at a long-term time scale (i.e., monthly or yearly).

2.2. Parameter optimization scheme

In the SiTHv2 model, the soil layer is extended to a total depth of 5 m, to better accommodate the root zone of forest. Thus, we re-optimized two critical parameters, D50 and D95, which are fundamental for representing at least 50% or 95% of the root system above the depth of D50 or D95, respectively. Based on the observed ET at each eddy covariance (EC) flux station, we used the differential-evolution Markov chain (DE-MC) algorithm (Ter Braak and Vrugt, 2008) to obtain the posterior distribution of D50 and D95 globally. In general, the posterior distribution of the candidate parameter sets (ϕ) in a Bayesian framework can be expressed as:

$$f\left(\phi \mid ET_{obs}\right) = f(\phi)\prod_{t=1}^{T}\frac{1}{\sqrt{2\pi\sigma^2}}\exp\left(-\frac{\left(ET_{sim}(\phi;t) - ET_{obs}(t)\right)^2}{2\sigma^2}\right) \quad (13)$$

where $f(\phi)$ represents the prior parameter distributions; $f(\phi \mid ET_{obs})$ represents the posterior parameter distributions; t is the time step (i.e., days); T is the total number of observations/simulations; ET_{obs} is the observed ET data at the flux station; ET_{sim} is the simulated ET from the SiTHv2 model; and σ is the standard deviation of the model error. In the DE-MC algorithm, the parameter proposals (ϕ_p) are generated based on two randomly selected chains (ϕ_{r1} and ϕ_{r2}), and the difference is multiplied by a scaling factor (ρ) and added to the current chain (ϕ_i):

$$\phi_p = \phi_i + \rho\left(\phi_{r1} - \phi_{r2}\right) + e \quad (14)$$

where the scaling factor ρ can be set to $2.38\sqrt{2d}$, and d is the dimension of parameter sets; and e is selected from a symmetrical distribution and represents a probabilistic acceptance rule in the DE-MC algorithm.

Specifically, in this study, we performed 12 chains in parallel with a total of 10000 iterations, including a burn-in time of 500 iterations. During the optimization, five-fold cross-validation was utilized in the

parameter optimization approach. The flux data were divided into five subsamples, with one subsample preserved as the data for validating the model, while the remaining four subsamples were used as the target function. This cross-validation procedure was repeated five times, and the results were then averaged to obtain an optimal solution for each site. This strategy maximizes the data utilization and can mitigate the overfitting and selection bias in the optimization. In addition, we employed a double-optimization scheme to implement parameter optimization at the PFT scale. This means that the optimal solutions for each site were first optimized using the site-observed ET as the target, to achieve the best root-mean-square error at the site level (S-RMSE). The optimal parameters for the individual PFTs could then be determined based on the posterior distribution of the parameters closest to the obtained S-RMSE for a particular PFT (Zhang et al., 2019b). This procedure ensured that the optimized parameters were optimally balanced in each PFT-specific site, even though the length of the valid data varied from site to site. The estimated posterior distribution of D50 and D95 for the different PFTs are given in Appendix (Fig. A.1).

2.3. Model performance evaluation metrics

To ensure that the ET-related variables can reach equilibrium, a 50 year spin-up was carried out by repeating the forcing from 2001 to 2005 10 times. The model was then run at the end of the spin-up to generate the global ET estimates. We also employed several statistical metrics to quantify the model performance in this study. Among the different metrics, a Taylor diagram was used to show the differences between the SiTHv2 and SiTHv1 models across multiple flux sites and PFTs. In a Taylor diagram, the model performance can be characterized as a comprehensive indicator, the Taylor skill score (TS-score), which is based on the correlation coefficient (R) and the normalized standard deviation (Zhang et al., 2017). Thus, each point in a Taylor diagram can be scored as:

$$S = \frac{2(1 + R)}{\left[(\sigma_s/\sigma_o) + 1/\left(\sigma_s/\sigma_o\right)\right]^2} \quad (15)$$

where S is the TS-score bounded by zero and unity, where unity represents perfect agreement with the observation; and σ_s and σ_o are the standard deviations of the simulation and observation, respectively. The root-mean-square error (RMSE) and the Nash–Sutcliffe efficiency coefficient (NSE) were also included in the statistical analysis for the comparison of the various ET models/products. These metrics are calculated as follows:

$$RMSE = \sqrt{\frac{1}{T}\sum_{t=1}^{T}[O(t) - M(t)]^2} \quad (16)$$

$$NSE = 1 - \frac{\sum_{t=1}^{T}[O(t) - M(t)]^2}{\sum_{t=1}^{T}[O(t) - \bar{O}]^2} \quad (17)$$

where $O(t)$ and $M(t)$ are the observed and simulated data at time t, respectively; and $\bar{O}$ is the mean value of the observed data. In general, the better the model performance, the lower the value of the RMSE and the closer the NSE value is to 1.

3. Data

3.1. Eddy covariance data

We used the observed meteorological and flux data from 175 EC stations globally (see Table S1 in the Supplementary information) to optimize the candidate parameters and evaluate model performance at the plot scale. These data were obtained from the FLUXNET2015 dataset (Pastorello et al., 2020) and contain 12 kinds of major PFTs under different climate zones (Fig. 3). It should be noted that quality control of the flux data is necessary before using these data in the parameter optimization procedure. The flux data (half-hourly) were
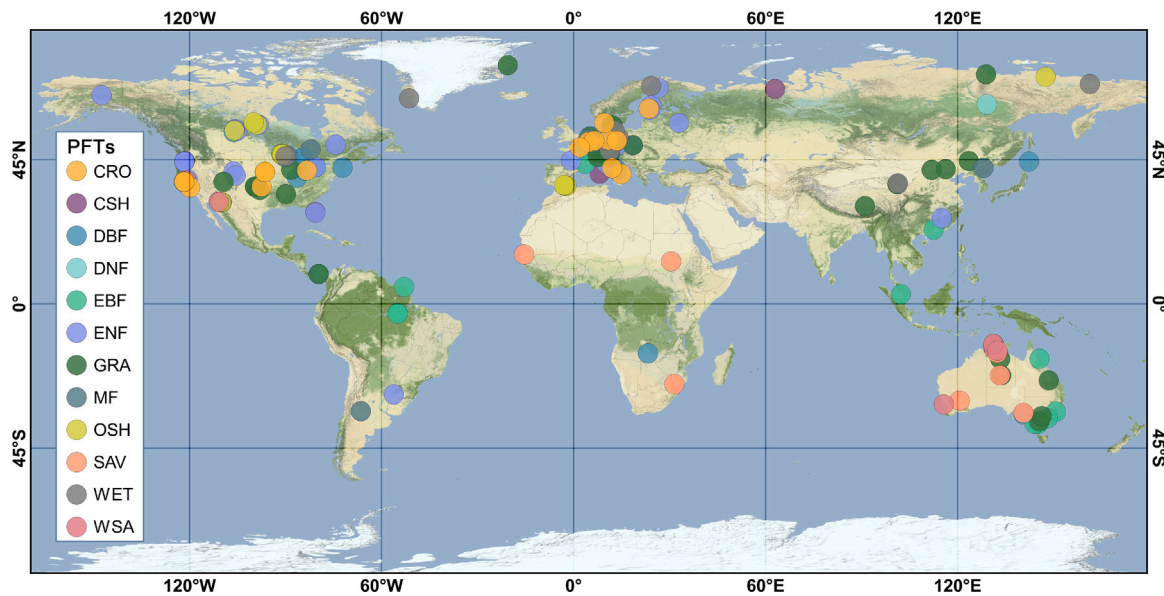
Fig. 3. Global distribution of the EC stations used in this study. The PFTs are according to the International Geosphere–Biosphere Programme (IGBP) ecosystem surface classification system. CRO: croplands; CSH: closed shrublands; DBF: deciduous broadleaf forest; DNF: deciduous needleleaf forest; EBF: evergreen broadleaf forest; ENF: evergreen needleleaf forest; GRA: grasslands; MF: mixed forest; OSH: open shrublands; SAV: savannas; WET: wetland; WSA: woody savannas.

considered missing in this study if the energy balance residual term (i.e., the net radiation minus the sum of the latent heat, sensible heat, and geothermal heat) exceeded 300 W m^{-2}. Linear interpolation was performed on the missing data if the data gap was less than 6 h in a day. After the pre-processing step, the quality of the EC data used in this study was strictly corrected, which ensured that the energy closure was generally above 70% at all the different PFTs. Finally, the flux data for each selected EC station were processed to a daily time series.

3.2. Inputs of the SiTHv2 model for global application

3.2.1. Remote sensing data

The dynamics of land vegetation are important to determine the energy partitioning when estimating terrestrial ET. To characterize the variation of vegetation growth, the LAI dataset (Version 50) from the Global Land Surface Satellite (GLASS) product (Liang et al., 2021) was used in this study. This LAI dataset was initially developed from Moderate Resolution Imaging Spectroradiometer (MODIS) data with a spatial resolution of 0.05° for the period of 2001–2018. Furthermore, to depict the vegetation water content in the SiTHv2 model, we used a VOD product from the VOD Climate Archive (VODCA), which is based on microwave observations from multiple sensors and can be divided into different spectral bands (Moesinger et al., 2020). The 0.25° daily X-band VODCA product with a continuous coverage from 2001 to 2018 was used in this study.

The land surface net radiation data used in this study were derived from the Clouds and the Earth's Radiant Energy System (CERES) project, which provides satellite-based observations of the Earth's radiation budget (Kato et al., 2018). Specifically, we selected the synoptic top of atmosphere (TOA) and surface fluxes and clouds (SYN) product and calculated the net surface radiation from the Level 3 SYN1deg dataset with the up/down shortwave/longwave flux. In addition, the global dynamic PFT distribution was obtained from the MODIS land-cover product (MCD12C1) with a spatial resolution of 0.05° globally (Sulla-Menashe et al., 2019). The main types of PFTs in the MCD12C1 product are in accordance with the International Geosphere–Biosphere Programme (IGBP) land-cover classification system. The details of the selected remote sensing data are summarized in Table 1.

3.2.2. Meteorological and ancillary data

The meteorological variables in the SiTHv2 model, including the 2-m air temperature (T_a), surface air pressure (P_a), and the total precipitation (P_{tot}), were obtained from the ERA5L product (Muñoz-Sabater et al., 2021) produced by the ECMWF at a spatial resolution of 0.1°. The original half-hourly ERA5L product was selected in this study, followed by aggregation to a daily scale to match the temporal interval in the SiTHv2 model. The global soil type map used in the SiTHv2 model was derived from the Harmonized World Soil Database (HWSD) v1.2 (Wieder et al., 2014), which combines the available soil information from regional and national institutes worldwide and provides a soil raster database with a 30 arc-second resolution.

3.3. Water balance based evapotranspiration data

In addition to evaluating the estimates of terrestrial ET at selected flux sites, we also used independent ET estimates to test the SiTHv2 model at a basin scale. The water-balanced evapotranspiration estimates (ET_{wb}) were generated from the residual of the water balance equation:

$$ET_{wb} = P - R - \Delta S \tag{18}$$

where P is the annual precipitation (mm year^{-1}); R is annual runoff for each basin; and ΔS is the changes in terrestrial water storage. A total of 49 basins from Ma et al. (2021) were selected, which represent a broad range of climate zones and PFTs. The precipitation data were acquired from the Global Precipitation Climatology Center (GPCC) Full Data Monthly Product Version 2018 (Schneider et al., 2018) for most basins, while the Parameter-elevation Regressions on Independent Slopes Model (PRISM) precipitation data (Daly et al., 2008) were used for basins in the continental United States because the PRISM product is considered to be the most accurate precipitation product for the United States (Lundquist et al., 2015). The measured runoff data for these basins were obtained from the Global Runoff Data Center, the China Sediment Bulletin, and the United States Geological Survey. The ΔS was extracted from the Gravity Recovery and Climate Experiment data (GRACE, RL06M, Version 2.0) released by the Jet Propulsion Laboratory (Wiese et al., 2016).

Table 1
Summary of selected remote sensing products in current study.

Variable	Product	Version	Spatial resolution	Period[a]	Reference
LAI	GLASS	V50	0.05°	2001–2018	Liang et al. (2021)
VOD	VODCA	X-Band	0.25°	2001–2018	Moesinger et al. (2020)
Radiation	CERES	SYN1deg(L3)	1°	2001–2018	Kato et al. (2018)
Landcover	MODIS	MCD12C1	0.05°	2001–2018	Sulla-Menashe et al. (2019)

[a]The time span shown here indicates the period used in the current study.

Table 2
Primary global terrestrial ET products used in this study for comparison.

ID[a]	Category	Theory	Spatial resolution	Time span	Reference
GLEAM	v3.5a	Remote sensing based model	0.25°	1980–2020	Martens et al. (2017)
CR	v1.0	Complementary relationship	0.25°	1982–2016	Ma et al. (2021)
FluxCom	All ensembles[b] in RS_METEO	Machine learning	0.5°	2001–2013	Jung et al. (2019)
CMIP6	Ensemble mean of 20 models[c]	Earth system model	0.5°	1979–2014	Eyring et al. (2016)
GLDAS	v2.1/Mosaic LSM	Land surface model	1°	1979–2020	Rodell et al. (2004)
ERA5L	The 5th generation (land component)	Reanalysis/land surface model	0.1°	1950–2021	Muñoz-Sabater et al. (2021)

[a]ID used in this study.

[b]All the ensembled latent heat flux estimates of 36 members with energy balance correction.

[c]Details of the 20 ESMs are provided in the Supplementary information (Table S2).

3.4. Comparative mainstream global ET products

Six mainstream terrestrial ET products were selected to compare with the ET estimates of the SiTHv2 model at a global scale. The terrestrial ET products used in this study were mainly derived from: (1) the Global Land Evaporation Amsterdam Model (GLEAM), which is a widely used process-based ET model (Martens et al., 2017); (2) the calibration-free complementary relationship (CR) model, which is driven by meteorological forcing and is used to calculate ET from the point view of atmospheric scope (Ma et al., 2021); (3) the FLUX-COM initiative product, which is estimated based on flux observations throughout the globe and a data-driven machine learning method (Jung et al., 2019); (4) the Global Land Data Assimilation System (GLDAS), which was developed to assimilate multi-source observations and simulations of land surface models to generate credible surface states and fluxes (Rodell et al., 2004); and (5) ERA5L, which is a cutting-edge global reanalysis product with a 0.1° spatial resolution and half-hourly temporal interval (Muñoz-Sabater et al., 2021). Notably, the ET products selected in this study were the most representative models or products among the different types of ET estimates.

We also used ET simulations from the ensemble mean of the 20 Earth system models in the Coupled Model Intercomparison Project Phase 6 (CMIP6) (Eyring et al., 2016), which is a mission led by the World Climate Research Programme. In contrast to the above-mentioned global ET products, these ET simulations were derived by an online Earth system, instead of meteorological forcing. The details of these selected products are provided in Table 2.

4. Results and discussions

4.1. ET validation at the plot scale using ET observations

We validated the ET estimates of the SiTHv2 model at the 175 flux stations and compared the results to those of the SiTHv1 model. The Taylor diagrams show the validation results for all the individual sites (Fig. 4a) and for the different PFTs (Fig. 4b). Moreover, the TS-score was used for scoring the model performance, which is a comprehensive indicator derived from the statistics of model errors (Zhu et al., 2016).

Despite the comparable correlation coefficient ranges, the SiTHv2 model is closer to 1 in terms of the normalized standard deviation (N-std) than the SiTHv1 model (Fig. 4a). The violin plots in the bottom panel demonstrate that the 25th to 75th percentile range of the TS-score for the SiTHv1 model is 0.71 to 0.89, with a median value of 0.82, whereas the 25th to 75th percentile range of the TS-score for the

SiTHv2 model is 0.82 to 0.93, with a median value of 0.88. Thus, when all 175 global flux stations are used as a benchmark, the estimated ET of the SiTHv2 model is more in line with the observations, and the TS-score of the SiTHv2 model is approximately 7.3% more than that of the SiTHv1 model. Furthermore, we also aggregated the ET estimates to the PFT scale to test the model performance between SiTHv1 and SiTHv2. Fig. 4b demonstrates that the correlation between the estimated ET of the SiTHv2 model and the observed ET in the various PFTs is stronger than that of the SiTHv1 model (except for EBF and SAV), with R-values ranging from 0.80 to 0.90. In addition, the results of the SiTHv2 model are more concentrated around the arc with N-std = 1, indicating that the ET estimates of the SiTHv2 model are closer to the average of the observations.

Furthermore, at least one representative site from each PFT was selected to demonstrate the superiority of the SiTHv2 model with multi-year monthly averages, which can make the contrast in the seasonal variations in model performance even more clearer. As shown in Fig. 5, it is evident that the SiTHv2 model improves the ET estimation to various extents for the different PFTs, with the reduction of RMSE values ranging from 16.5% (RU-SkP, from 9.52 to 7.95 mm month^{-1}) to 68.9% (CN-HaM, from 13.36 to 4.15 mm month^{-1}). This is mostly due to the modified soil water constraint scheme implemented in the SiTHv2 model, which accounts for the influence of VOD and the relocation of roots in different soil layers, thereby reducing the over-estimation of the old version in most cases.

To further demonstrate the performance of the new version (SiTHv2), we ran the PT-JPL model (Fisher et al., 2008) and the MOD16 model (Mu et al., 2011) on these selected sites and calculated their performance at the PFT level separately (different colored backgrounds) as a side-by-side comparison, in addition to the internal comparison between SiTHv2 and SiTHv1. As shown in Fig. 6, the performance of the different models shows a high degree of PFT-specific variation, which can be attributed to the different model structures. Among the different models, the RMSE of the SiTHv2 model is generally the smallest across the 12 kinds of PFTs, compared to the other models, with the median values ranging from 0.48 to 0.83 mm day^{-1}. The average median value of the RMSE in all the PFTs for the SiTHv2 model is 0.66 mm day^{-1}, while that for the SiTHv1 model is 0.90 mm day^{-1}, which suggests that the overall accuracy of the SiTHv2 model is improved by around 27% when compared to the SiTHv1 model, in terms of RMSE statistics. Furthermore, the performance of the PT-JPL model is close to that of the SiTHv2 model in most PFTs, with an average RMSE median value of 0.82 mm day^{-1}. Meanwhile, the MOD16 model shows a wide range of variability across the multiple PFTs, with the median value of the RMSE
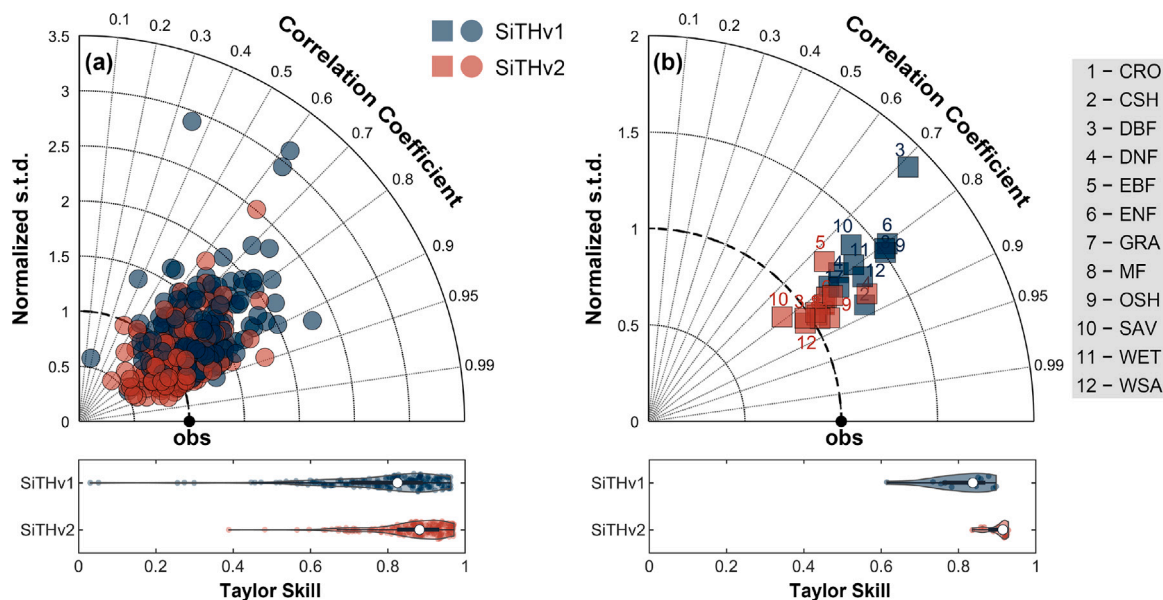
Fig. 4. Validation of the ET estimates of the SiTHv2 and SiTHv1 models at individual sites (a) and at the PFT scale (b). The *y*-axis indicates the normalized standard deviation (N-std) with observed values as the target, the arcs represent Pearson correlation coefficients (*R*), and the black dot on the *x*-axis represents the observed benchmark value.
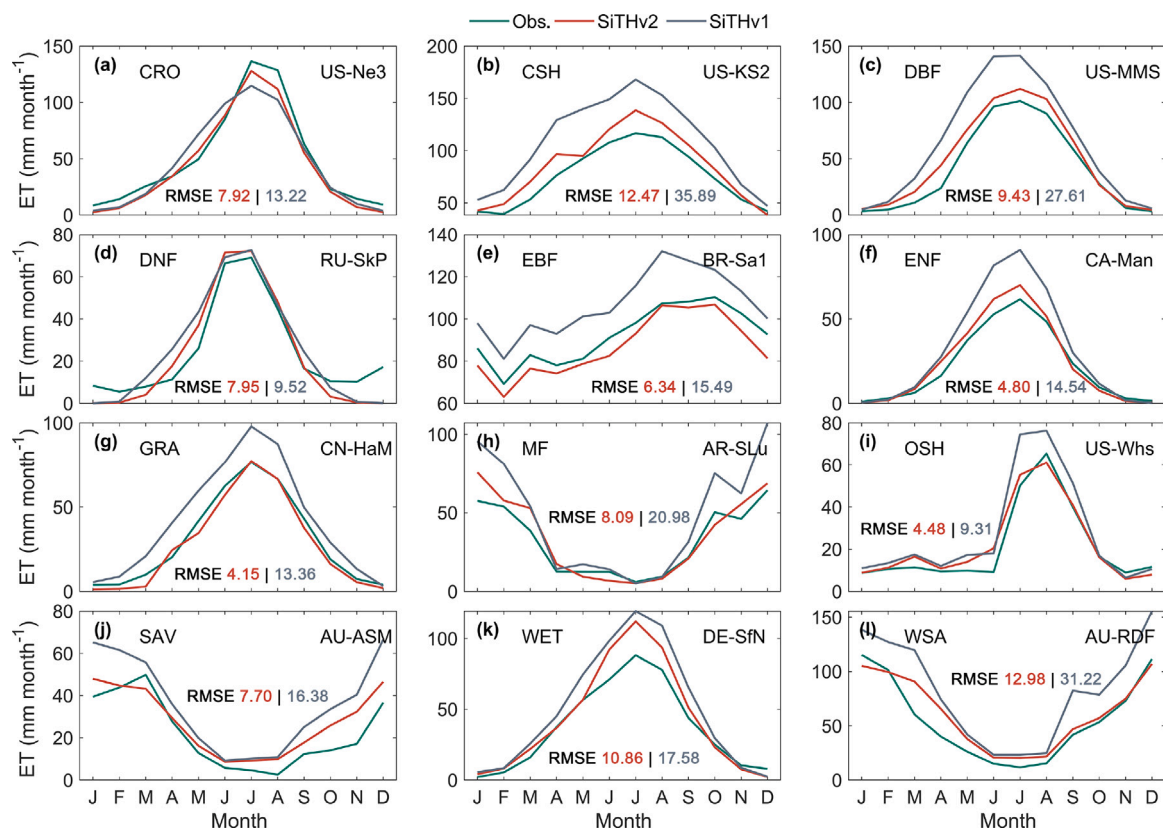

Fig. 5. Comparison of the model improvements for typical sites in different PFTs. The green line is the observed ET at each flux site, while the red and gray lines represent the outcomes of the SiTHv2 and SiTHv1 models, respectively. (For interpretation of the references to color in this figure legend, the reader is referred to the web version of this article.)

ranging from 0.62 to 1.29 mm day^{-1}, despite it performing better in the DBF and EBF areas.

Consequently, based on the ground benchmark of EC observations from a total of 175 flux stations, it is confirmed that the SiTHv2 model can provide more accurate ET estimates across the different PFTs, compared to the SiTHv1 model, and it also performs well when compared with the PT-JPL and MOD16 models.

4.2. ET validation at the basin scale using ET_{wb}

Unlike the use of ground-based data to validate the performance of models at the plot scale, the grid-based terrestrial ET estimates are commonly subject to the limitation of the uncertainty for the scale effect, which is caused by the spatial mismatch between the simulated ET grid and the ground-based flux footprint. Therefore, we used the
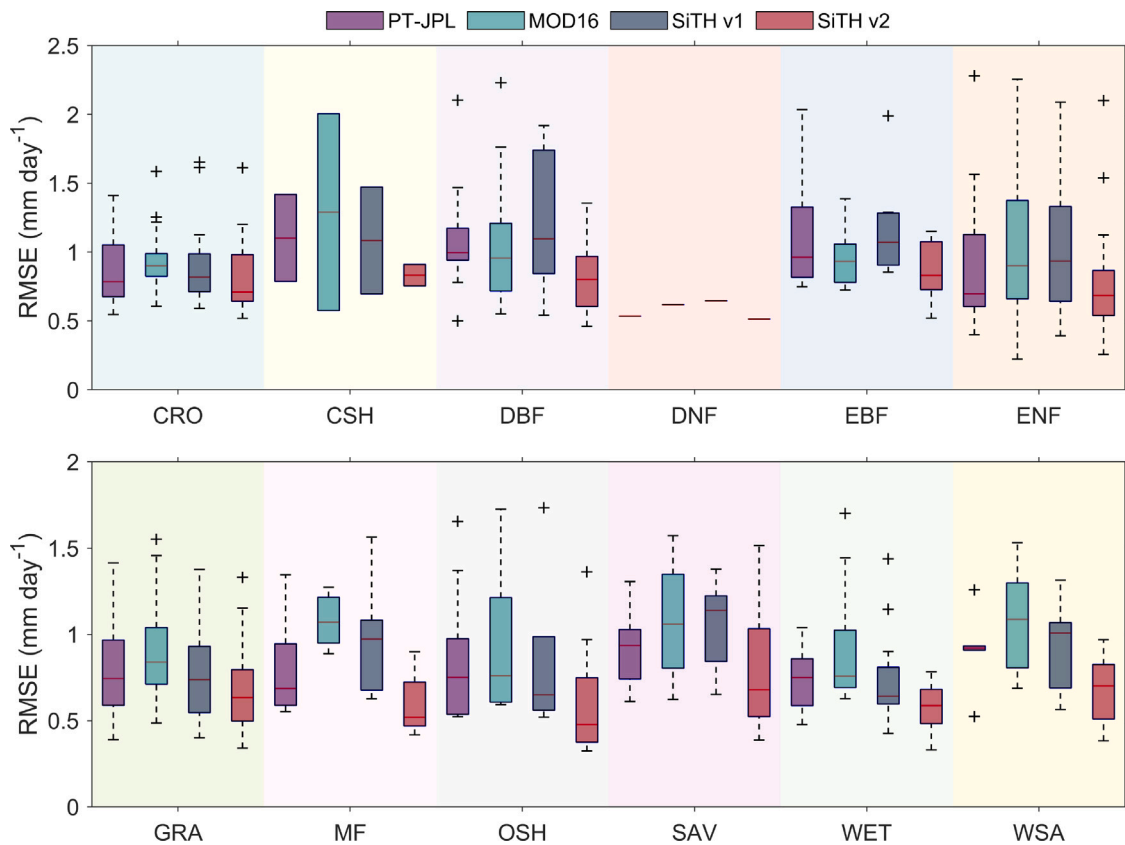
Fig. 6. Box plots of the RMSE values when evaluating the modeling results of the SiTHv2, SiTHv1, MOD16, and PT-JPL models against 175 EC stations in different plant functional types.
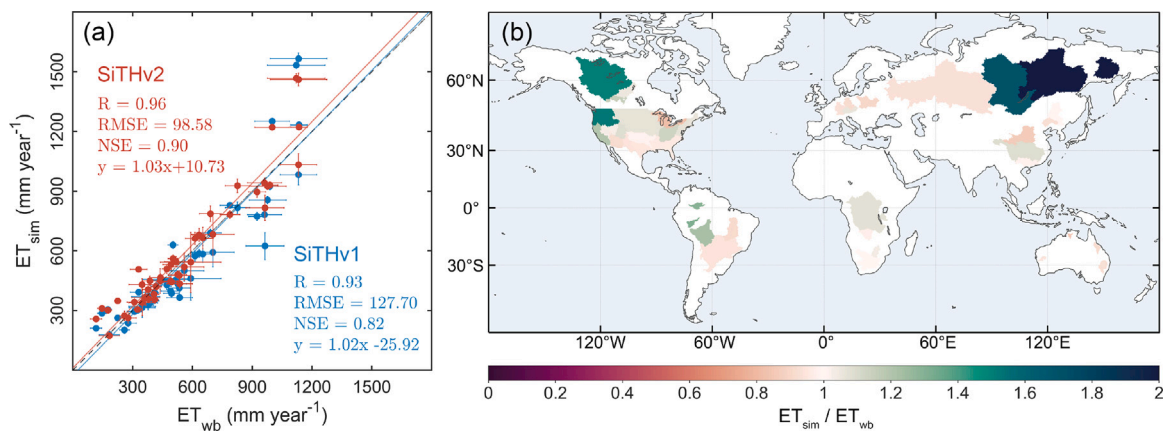

Fig. 7. Evaluation of the simulated ET (ET_{sim}) from the SiTHv2 model based on the water-balanced ET (ET_{wb}) at 49 basins over the period of 2003 to 2013 (the same overlapping time span as the other ET products in Fig. 8). (a) Scatter plot between the ET_{sim} and ET_{wb} with statistics. The unit of RMSE is mm year^{-1}. (b) The spatial distribution of the multi-year averaged ET rates relative to the ET_{wb} of the 49 basins. (For interpretation of the references to color in this figure legend, the reader is referred to the web version of this article.)

independent water-balanced ET data to validate the generated ET outputs at the basin scale. As described in Section 3.4, the magnitude of the ET in the major global basins was derived from the water balance equation, based on ground or remotely sensed observations of runoff, precipitation, and changes in terrestrial water storage.

Fig. 7a illustrates the scatter plot linear regression between the ET estimates of the SiTHv2 model (red) and SiTHv1 model (blue) for these basins against the water-balanced ET (ET_{wb}) over the period from 2003 to 2013. It can be found that the ET estimated by the SiTHv2 model is generally more consistent with the ET_{wb} than that estimated by the SiTHv1 model, with a higher correlation ($R = 0.96$) and smaller

deviation (RMSE = 98.58 mm·year^{-1}). Furthermore, the SiTHv2 model shows an improvement of nearly 0.1 compared to the SiTHv1 model in terms of the Nash–Sutcliffe model efficiency coefficient (NSE).

The ratio of the simulated ET (SiTHv2) to ET_{wb} was also calculated to highlight the spatial distribution of the over- or under-estimation of the ET estimates, with ET_{wb} as the benchmark. In the majority of basins, the difference between the estimated ET obtained by the SiTHv2 model and ET_{wb} is fairly minimal, with ratios ranging from 0.8 to 1.2. Meanwhile, it can be found that the ET estimated by the SiTHv2 model exhibits a certain degree of over-estimation, of up to double the corresponding ET_{wb} in basins at high latitudes in the Northern Hemisphere
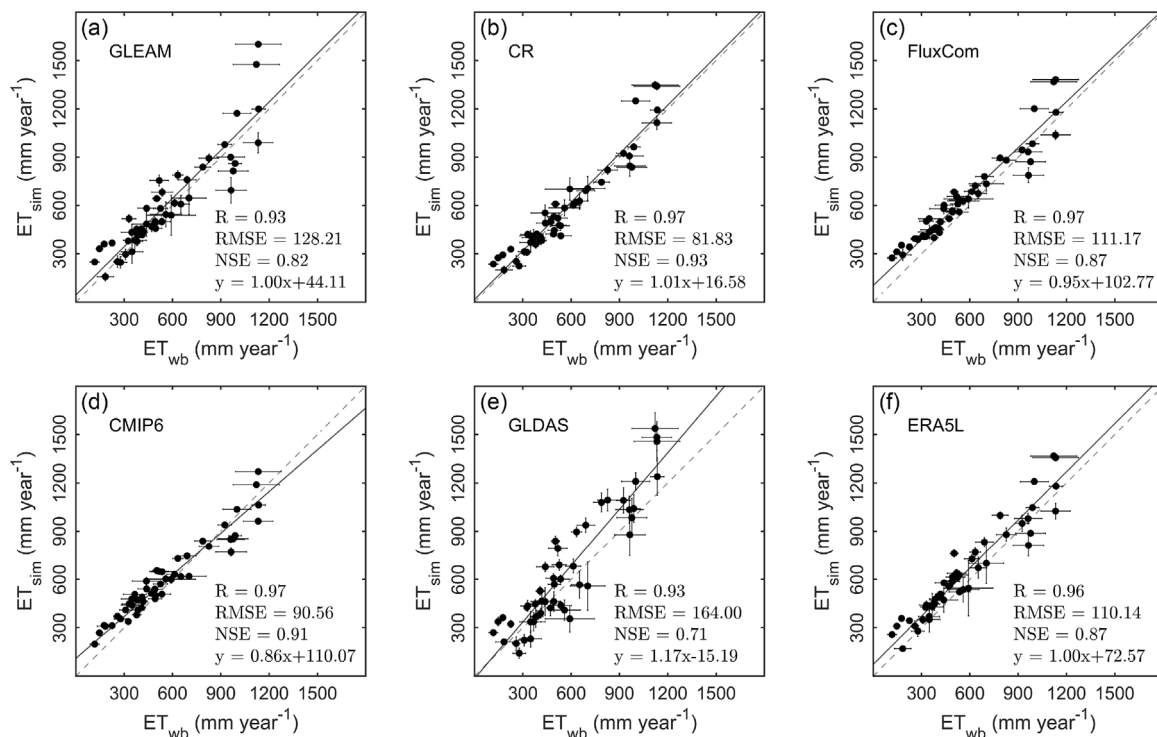
Fig. 8. Regression plots of the yearly simulated ET rates from the six primary global ET products relative to the ET_{wb} at 49 basins during their overlapping temporal coverage from 2003 to 2013. The length of the error bar represents the interannual variability of the ET in each basin. The gray dashed line represents the 1:1 line, while the black line shows the regression line, with the corresponding regression equation shown in the bottom.

(e.g., Siberia and Northern Canada). Indeed, the freeze-thaw processes at high latitudes have a direct effect on soil water content, which in turn influences the ET process (Niu and Yang, 2006). However, the current process-based ET model lacks a meaningful connection of the freeze-thaw process and the vast amount of measurable data for calibration (such as subsurface ice), which makes accurate estimation of ET in these specific regions a challenging task.

Moreover, we also selected six mainstream global terrestrial ET products for a side-by-side comparison with the SiTHv2 model at the basin scale (Fig. 8). The correlation relationship (R) between all the ET products and ET_{wb} is very high, with a range of 0.93 to 0.97, which indicates the good consistency in the spatial variability of these ET products across the selected basins. However, the accuracies of these ET products are relatively diverse, with the GLDAS product having the largest RMSE (164 mm year^{-1}) and the smallest NSE (0.71). In contrast, the CR product performs the best, with the smallest RMSE (81.83 mm year^{-1}) and the largest NSE (0.93) among these products, which are similar results to those of the SiTHv2 model obtained in this study. Meanwhile, the FluxCom ET product was produced using substantial ground-based flux data with machine learning technology, and shows high correlation ($R = 0.97$) with the derived ET_{wb} across the different basins. However, this product shows some over-estimation for ET_{wb} in the basins with an arid or cold climate, which are often characterized by low ET values. The performance of the GLEAM product is similar to that of the SiTHv1 model, with an RMSE value of 128.21 mm year^{-1} and an NSE value of 0.82. However, the results of the GLEAM product are significantly higher than the results of the other models in basins with a humid climate (e.g., the Amazon region), where the maximum value exceeds 1500 mm year^{-1}. In terms of statistical indicators, the CMIP6 product's RMSE (90.56 mm year^{-1}), R (0.97), and NSE (0.91) values are in the upper-middle level in the overall range, but the lowest slope (0.86) and the largest intercept (110.07 mm year^{-1}) are found among these model statistics. This indicates that the ET estimates of the CMIP6 product are significantly under-estimated at high values and over-estimated at low values in these basins. The

results of the ERA5L product also yield a relatively high NSE value (0.87) and an RMSE value of 110.14 mm year^{-1}, which are similar to the results of the FluxCom product. Nevertheless, despite the ERA5L product achieving a slope value of 1, its intercept is rather large (72.57 mm year^{-1}), implying an overall over-estimation in these 49 basins, relative to ET_{wb}.

It is necessary to emphasize that the different spatial resolutions and production methods of these global ET products lead to differences in capturing the spatial details of terrestrial ET, although their statistical metrics are similar at the basin scale. In general, the terrestrial ET estimated by the SiTHv2 model is in good agreement with the ET_{wb} at the basin scale, and the performance is also at a superior level when compared to the primary global ET products available at present.

4.3. Global comparison of ET magnitude and trend analysis

The global distribution of the multi-year (2001–2018) mean ET estimated by the SiTHv2 model is displayed in Fig. 9a. The estimated terrestrial ET exhibits a clear and reasonable geographical distribution, with the maximum ET appearing in the tropics around the equator (1200–1500 mm year^{-1}), followed by the temperate humid regions (600–1200 mm year^{-1}), and then the alpine and high-latitude areas (300–600 mm year^{-1}), and the lowest ET is found in the desert and ice regions (< 100 mm year^{-1}). The latitudinal profile of the estimated ET derived by the SiTHv2 model is in close agreement with the highest confidence curve (Fig. 9b), which indicates that the SiTHv2 model is effective in capturing the variance in global terrestrial ET at different latitudes. However, the ET profile estimated by the SiTHv2 model is positioned lower than that of the other ET models in regions south of 40 °S. This may be related to the increased uncertainty of the ERA5-based precipitation in South America (Xiong et al., 2022), especially since the assimilation system hardly corrects the systematic bias in the solid precipitation (i.e., snowfall), due to the insufficient observations (Muñoz-Sabater et al., 2021).
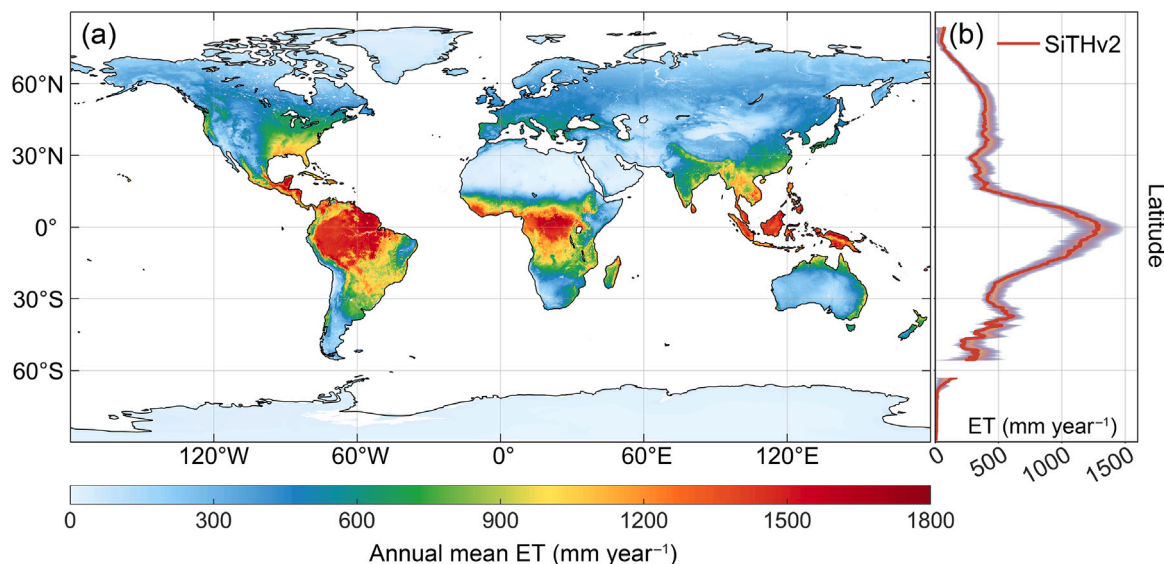
Fig. 9. (a) Spatial distribution of the multi-year average terrestrial ET from 2001 to 2018. (b) The latitude-averaged profile of the terrestrial ET corresponds to the panel, where the red line represents the estimates of the SiTHv2 model, and the background range is obtained from the selected primary global ET products (see Table 2), with the gradient color representing the confidence range (± standard deviation) of the different global ET products. (For interpretation of the references to color in this figure legend, the reader is referred to the web version of this article.)

At the global scale, the magnitude of the total terrestrial ET estimated by the various global ET products is a crucial comparative indicator. To compare the estimated terrestrial ET volumes, we used the overlapping period from 2001 to 2013, which covers the time span for both the SiTH-based ET estimates and the other ET products. As shown in Fig. 10a, the SiTHv2 model estimates a total annual mean terrestrial ET of $70.3 \pm 0.6 \times 10^3$ km^3, which is very close to the GLEAM estimate ($70.4 \pm 0.8 \times 10^3$ km^3) and represents a 6.4% increase over the SiTHv1 model ($66.1 \pm 0.6 \times 10^3$ km^3). The results of these three datasets, together with CMIP6, are lower than the average value (71.5×10^3 km^3) of all the selected global ET products, whereas the estimated ET of the remaining four products is higher than the average value, with the CR ($73.0 \pm 0.7 \times 10^3$ km^3) and GLDAS ($72.1 \pm 3.7 \times 10^3$ km^3) products being closest to the average, and the FluxCom product occupying the highest position ($77.6 \pm 0.3 \times 10^3$ km^3). In comparison, the reported volume of the terrestrial ET derived from the different models/products in previous studies has primarily ranged from 65×10^3 km^3 to 75×10^3 km^3, with individual values of 65.5×10^3 km^3 (Oki and Kanae, 2006), 65×10^3 km^3 (Jung et al., 2010), 67.9×10^3 km^3 (Miralles et al., 2011), 74.3×10^3 km^3 (Zhang et al., 2015), 72.8×10^3 km^3 (Zhang et al., 2019a), and 71.1×10^3 km^3 (Zeng et al., 2014). More recent studies have tended to yield ET volumes in excess of 70×10^3 km^3. Furthermore, the energy balancing strategy seems to be more likely to estimate greater ET volumes, with the magnitude of the global terrestrial ET estimate being up to around 75×10^3 km^3 (Jung et al., 2019; L'Ecuyer et al., 2015; Wild et al., 2015). In addition, it is worth noting that the time span of the above-mentioned ET statistics varies across the different studies.

We divided the global terrestrial ET estimates into five main types based on the Köppen climate classification system (see Fig. S1 in the Supplementary information), namely, tropical zone, dryland zone, temperate zone, continental zone, and polar and alpine zone, to compare the differences of the multiple global ET products under the different climatic conditions over the globe. The ET volumes estimated by the different products are more or less equivalent to the average value ($32.6 \pm 1.4 \times 10^3$ km^3) in the tropical zone (Fig. 10b), except for the CMIP6 product, which displays obvious under-estimation ($29.6 \pm 0.1 \times 10^3$ km^3). However, the performance of the different ET products in the arid zone varies considerably (Fig. 10c), among which the ET estimate from the FluxCom product ($12.9 \pm 0.2 \times 10^3$ km^3) is the highest, compared to the

others. The ERA5L and CR products obtain comparable ET volumes in the dryland zone (around $10 \pm 0.6 \times 10^3$ km^3 to $10.5 \pm 0.4 \times 10^3$ km^3), while the result of the SiTHv2 model is similar to that of the GLEAM product, with $8.8 \pm 0.5 \times 10^3$ km^3. Unlike the tropical zone, it is interesting to note that the ET estimate of the CMIP6 product is the second highest for the dryland zone, at $12.5 \pm 0.1 \times 10^3$ km^3.

For the temperate zone (Fig. 10d), the ERA5L product shows the highest ET estimate ($16.3 \pm 0.2 \times 10^3$ km^3), whereas the lowest ET volume is estimated by the SiTHv1 model ($13.5 \pm 0.1 \times 10^3$ km^3). The ET estimates from the FluxCom and GLDAS products in the temperate zone are much higher than the overall average, with values of $16 \pm 0.1 \times 10^3$ km^3 and $15.7 \pm 0.7 \times 10^3$ km^3, respectively. However, the ET estimates from the GLEAM, CR, and CMIP6 products and the SiTHv2 model are substantially lower, ranging from $14.5 \pm 0.1 \times 10^3$ km^3 to $15.0 \pm 0.2 \times 10^3$ km^3. In the context of continental climatic conditions with considerable daily and annual air temperature variations, the SiTHv1 model tends to under-estimate the volume of ET ($10.6 \pm 0.2 \times 10^3$ km^3), compared to the other terrestrial ET products (Fig. 10e). In the SiTHv2 model, the estimated total ET for the continental climate zone is $11.8 \pm 0.3 \times 10^3$ km^3, which is comparable to the $11.5 \pm 0.1 \times 10^3$ km^3 for the CR product and the $11.7 \pm 0.1 \times 10^3$ km^3 for the CMIP6 product. The four remaining products generally estimate higher ET values exceeding the average ($12.2 \pm 0.9 \times 10^3$ km^3) in the continental climate zone, ranging from $12.7 \pm 0.2 \times 10^3$ km^3 (GLEAM) to $13.2 \pm 0.2 \times 10^3$ km^3 (ERA5L).

Lastly, the total ET volume in the polar and alpine zone (Fig. 10f) is much lower than in the other zones, due to the reduced solar radiation, lower temperature, and lack of vegetation cover. Nonetheless, the various ET products exhibit a degree of variability, with the CMIP6 product yielding the highest ET volume of $2.3 \pm 0.01 \times 10^3$ km^3, and the smallest volume of ET is estimated by the SiTHv1 model ($1.47 \pm 0.01 \times 10^3$ km^3). The ET volume estimated by the SiTHv2 model ($1.93 \pm 0.02 \times 10^3$ km^3) for the polar and alpine zone is very close to that of the ERA5L product ($1.92 \pm 0.03 \times 10^3$ km^3). Comparatively, the GLEAM ($1.64 \pm 0.03 \times 10^3$ km^3), FluxCom ($1.68 \pm 0.003 \times 10^3$ km^3), and GLDAS ($1.67 \pm 0.1 \times 10^3$ km^3) products yield similar ET volumes that are slightly less than the overall average ($1.78 \pm 0.4 \times 10^3$ km^3) for this zone.

The trend of annual global terrestrial ET estimated by the SiTHv2 model from 2011 to 2018 is 0.41 mm year^{-1} ($p < 0.05$), while the trend for the SiTHv1 model is 0.38 mm year^{-1} ($p < 0.05$) (Fig. 11). It should be emphasized that the valid periods for the comparable ET products
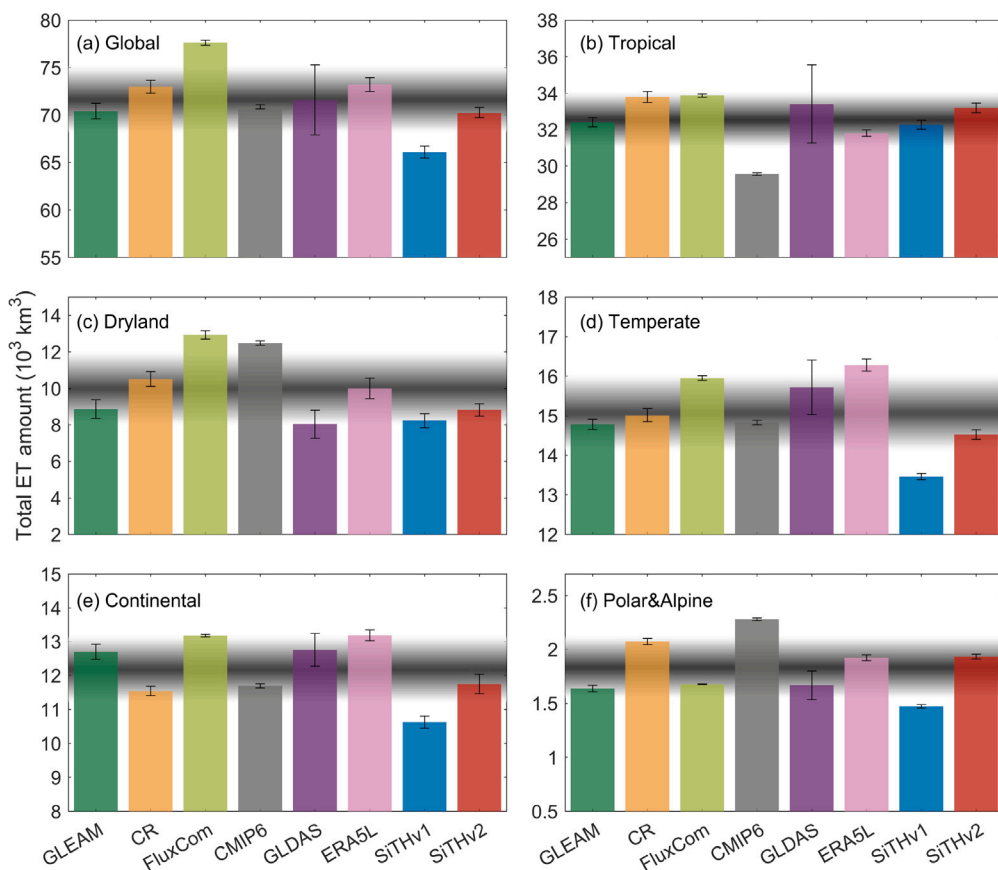
Fig. 10. Comparison of the multi-year average terrestrial ET volume for (a) the global scale, (b) the tropical zone, (c) the dryland zone, (d) the temperate zone, (e) the continental zone, and (f) the polar and alpine zone for the period of 2001 to 2013. The error bar represents the standard deviation of the annual values of the ET estimates for each product. The gray gradient range represents the mean of all the products plus/minus their standard deviations. The climate zone classification is in accordance with the Köppen climate classification system.
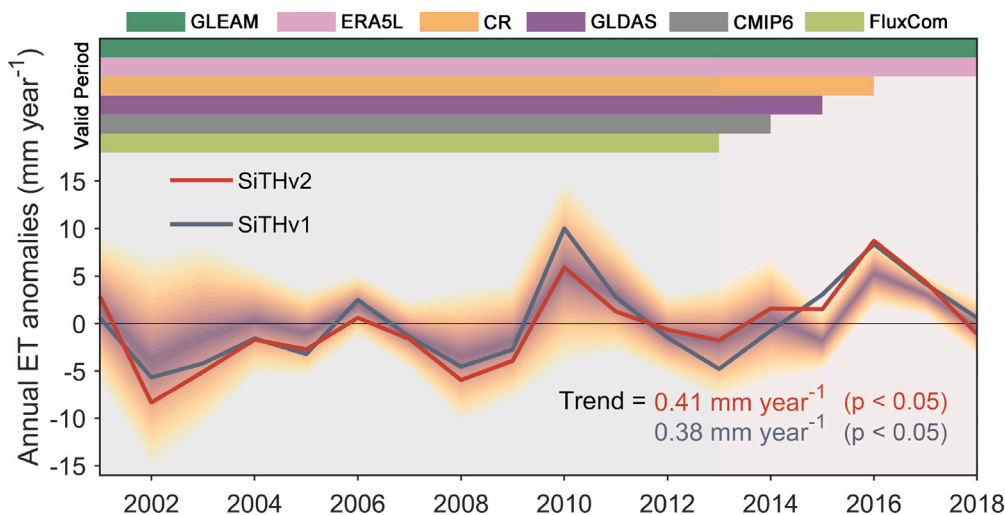

Fig. 11. Trends in global terrestrial ET from 2001 to 2018. The red line and gray line represent the trend of the ET anomalies from the SiTHv2 and SiTHv1 models, respectively. The gradually varied interval is the confidence range of the ensemble mean values derived from the multiple ET products, except for SiTH, and the upper panel indicates the valid periods for the products used in this study. (For interpretation of the references to color in this figure legend, the reader is referred to the web version of this article.)

differ, and their overlapping period in this study spans from 2001 to 2013. As a result, the confidence interval shrinks after 2013 because of the decreased contribution from the various global ET products. Both versions of the SiTH model demonstrate a strong correlation with the ensemble mean of the multiple ET products (which excludes the SiTH-based ET estimates), indicating that the anomaly trend of the

SiTH-based ET is realistic, and can be used to achieve credible trend analysis for historical periods. Moreover, the SiTHv2 model is more consistent with the ensemble mean value of the multiple ET products in the details, compared to the SiTHv1 model. In summary, the global terrestrial ET produced by the SiTHv2 model outperforms that of the SiTHv1 model, and the SiTHv2 model can provide reliable ET estimates
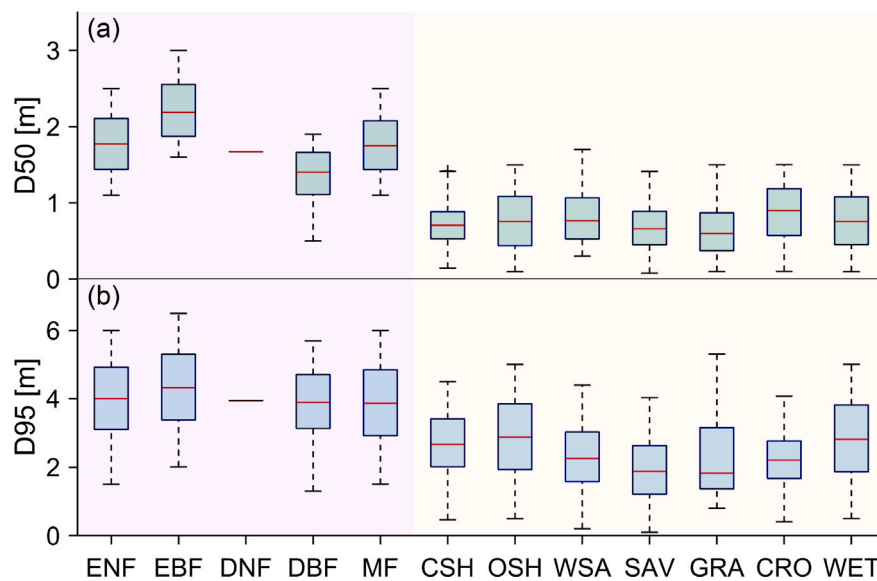
Fig. A.1. Posterior distributions of D50 and D95 in the different PFTs. The boxes represent the 75% credible interval, and the horizontal line represents the median value.

in terms of global spatial distribution, latitudinal profile, and multi-year ET volumes, for both a global scale and the various climate zones, as well as the anomaly trend of terrestrial ET.

Nonetheless, the SiTHv2 model still has some limitations and deficiencies that will require further enhancement in the next stage. Although the current spatial resolution reaches 0.1°, which is globally in line with the ERA5L product, a finer spatial resolution is important for local-scale applications. To this end, downscaling schemes such as sub-grid optimization could be an efficient way to generate finer ET estimates by combining the advantages of multi-source reanalysis and satellite forcing data with different spatial resolutions. Also, for the current version, the IWU is regarded as additional rainfall only loosely coupled to the SiTHv2 model, which can ensure water availability to irrigated regions at the monthly/yearly scale (limited by the monthly IWU estimates), but makes it difficult to characterize the irrigation recharge at a fine temporal scale. Together with the challenge of representing specific irrigation modes, i.e., sprinkler, drip, or flood irrigation, these factors will increase the uncertainty in the simulation of soil water dynamics. Hence, to assimilate satellite-based soil moisture into the simulation would be a more direct way of characterizing realistic surface water conditions, and further improving cropland ET estimation. In addition, the current model is only applied to the simulation in the vertical direction, without the interaction from the neighboring grids. By introducing topographic factors (e.g., elevation, slope, and aspect) to describe the lateral water flow between adjacent grid cells, this would enhance the simulation of the SiTHv2 model to three dimensions, and could thus greatly expand the application potential at the basin level.

5. Conclusions

This study was dedicated to improving the ET simulation in the SiTH model within the GSPAC. We enhanced the vegetation moisture constraint module by coupling satellite-based VOD measurements. Moreover, a dynamic adjustment scheme for the critical threshold of soil water content based on different canopy heights and specific environmental conditions was applied in the SiTHv2 model. The extended soil layer with re-optimized root distribution parameters was used to better characterize the effect of soil water dynamics on the ET simulation. We also added an irrigation water strategy as extra input water applied in the croplands zone. In addition, the meteorological forcing data in the SiTHv2 model were updated to the state-of-the-art ERA5L reanalysis product.

Validations against 175 EC stations and water balance data from 49 large river basins suggested that the SiTHv2 model is more accurate and has less uncertainty than the SiTHv1 model at both plot and basin scales. Further multi-product evaluations using the water balance approach also demonstrated that the SiTHv2 model ranks well when compared to most of the mainstream ET products. Lastly, a side-by-side comparison at the global scale indicated that the SiTHv2 model is consistent with the ensemble mean results of the multiple terrestrial ET products, both in terms of magnitude and trends. This newly improved SiTH model will provide the necessary framework for estimating ET from the GSPAC, and will promote better support for exploring land–atmosphere feedback loops, ecosystem water consumption, and related ecohydrological studies.

CRediT authorship contribution statement

Kun Zhang: Conceptualization, Methodology, Writing – original draft, Formal analysis, Funding acquisition. **Gaofeng Zhu:** Conceptualization, Writing – review & editing, Funding acquisition. **Ning Ma:** Writing – review & editing, Data curation. **Huiling Chen:** Methodology, Figure plotting. **Shasha Shang:** Writing – review & editing.

Declaration of competing interest

The authors declare that they have no known competing financial interests or personal relationships that could have appeared to influence the work reported in this paper.

Data availability

The generated global terrestrial ET dataset of the SiTHv2 model can be achieved from the National Tibetan Plateau Data Center (TPDC) at http://dx.doi.org/10.11888/Atmos.tpdc.272728.

Acknowledgments

Appendix A. Posterior distribution of D50 and D95

See Fig. A.1.

Appendix B. Supplementary data

Supplementary material related to this article can be found online at https://doi.org/10.1016/j.jhydrol.2022.128440.

References

Allen, R.G., Pereira, L.S., Howell, T.A., Jensen, M.E., 2011. Evapotranspiration information reporting: I. Factors governing measurement accuracy. Agricult. Water Manag. 98, 899–920. http://dx.doi.org/10.1016/j.agwat.2010.12.015.

Beer, A., 1852. Bestimmung der absorption des rothen lichts in farbigen flussigkeiten. Ann. Phys. 162, 78–88.

Canadell, J., Jackson, R.B., Ehleringer, J.B., Mooney, H.A., Sala, O.E., Schulze, E.-D., 1996. Maximum rooting depth of vegetation types at the global scale. Oecologia 108, 583–595. http://dx.doi.org/10.1007/BF00329030.

Chen, H., Zhu, G., Shang, S., Qin, W., Zhang, Y., Su, Y., Zhang, K., Zhu, Y., Xu, C., 2022. Uncertainties in partitioning evapotranspiration by two remote sensing-based models. J. Hydrol. 604, 127223. http://dx.doi.org/10.1016/j.jhydrol.2021.127223.

Chen, H., Zhu, G., Zhang, K., Bi, J., Jia, X., Ding, B., Zhang, Y., Shang, S., Zhao, N., Qin, W., 2020. Evaluation of evapotranspiration models using different LAI and meteorological forcing data from 1982 to 2017. Remote Sens. 12, 2473. http://dx.doi.org/10.3390/rs12152473.

Daly, C., Halbleib, M., Smith, J.I., Gibson, W.P., Doggett, M.K., Taylor, G.H., Curtis, J., Pasteris, P.P., 2008. Physiographically sensitive mapping of climatological temperature and precipitation across the conterminous United States. Int. J. Climatol. 28, 2031–2064. http://dx.doi.org/10.1002/joc.1688.

van Diepen, C., Wolf, J., van Keulen, H., Rappoldt, C., 1989. WOFOST: A simulation model of crop production. Soil Use Manag. 5, 16–24. http://dx.doi.org/10.1111/j.1475-2743.1989.tb00755.x.

Dorigo, W., Dietrich, S., Aires, F., Brocca, L., Carter, S., Cretaux, J.-F., Dunkerley, D., Enomoto, H., Forsberg, R., Güntner, A., Hegglin, M.I., Hollmann, R., Hurst, D.F., Johannessen, J.A., Kummerow, C., Lee, T., Luojus, K., Looser, U., Miralles, D.G., Pellet, V., Recknagel, T., Vargas, C.R., Schneider, U., Schoeneich, P., Schröder, M., Tapper, N., Vuglinsky, V., Wagner, W., Yu, L., Zappa, L., Zemp, M., Aich, V., 2021. Closing the water cycle from observations across scales: Where do we stand? Bull. Am. Meteorol. Soc. 102, E1897–E1935. http://dx.doi.org/10.1175/BAMS-D-19-0316.1.

Eyring, V., Bony, S., Meehl, G.A., Senior, C.A., Stevens, B., Stouffer, R.J., Taylor, K.E., 2016. Overview of the coupled model intercomparison project phase 6 (CMIP6) experimental design and organization. Geosci. Model Dev. 9, 1937–1958. http://dx.doi.org/10.5194/gmd-9-1937-2016.

Fan, Y., 2015. Groundwater in the Earth's critical zone: Relevance to large-scale patterns and processes. Water Resour. Res. 51, 3052–3069. http://dx.doi.org/10.1002/2015WR017037.

Fisher, J.B., Tu, K.P., Baldocchi, D.D., 2008. Global estimates of the land–atmosphere water flux based on monthly AVHRR and ISLSCP-II data, validated at 16 FLUXNET sites. Remote Sens. Environ. 112, 901–919. http://dx.doi.org/10.1016/j.rse.2007.06.025.

Foley, J.A., Ramankutty, N., Brauman, K.A., Cassidy, E.S., Gerber, J.S., Johnston, M., Mueller, N.D., O'Connell, C., Ray, D.K., West, P.C., Balzer, C., Bennett, E.M., Carpenter, S.R., Hill, J., Monfreda, C., Polasky, S., Rockström, J., Sheehan, J., Siebert, S., Tilman, D., Zaks, D.P.M., 2011. Solutions for a cultivated planet. Nature 478, 337–342. http://dx.doi.org/10.1038/nature10452.

Frankenberg, C., Fisher, J.B., Worden, J., Badgley, G., Saatchi, S.S., Lee, J.-E., Toon, G.C., Butz, A., Jung, M., Kuze, A., Yokota, T., 2011. New global observations of the terrestrial carbon cycle from GOSAT: Patterns of plant fluorescence with gross primary productivity. Geophys. Res. Lett. 38, http://dx.doi.org/10.1029/2011GL048738.

Gou, S., Miller, G., 2014. A groundwater–soil–plant–atmosphere continuum approach for modelling water stress, uptake, and hydraulic redistribution in phreatophytic vegetation. Ecohydrology 7, 1029–1041. http://dx.doi.org/10.1002/eco.1427.

Held, I.M., Soden, B.J., 2006. Robust responses of the hydrological cycle to global warming. J. Clim. 19, 5686–5699. http://dx.doi.org/10.1175/JCLI3990.1.

Impens, I., Lemeur, R., 1969. Extinction of net radiation in different crop canopies. Arch. Meteorol. Geophys. Bioklimatol. B 17, 403–412.

Jackson, T.J., Schmugge, T.J., 1991. Vegetation effects on the microwave emission of soils. Remote Sens. Environ. 36, 203–212. http://dx.doi.org/10.1016/0034-4257(91)90057-D.

Jasechko, S., Sharp, Z.D., Gibson, J.J., Birks, S.J., Yi, Y., Fawcett, P.J., 2013. Terrestrial water fluxes dominated by transpiration. Nature 496, 347–350. http://dx.doi.org/10.1038/nature11983.

Jung, M., Koirala, S., Weber, U., Ichii, K., Gans, F., Camps-Valls, G., Papale, D., Schwalm, C., Tramontana, G., Reichstein, M., 2019. The FLUXCOM ensemble of global land-atmosphere energy fluxes. Sci. Data 6, 74. http://dx.doi.org/10.1038/s41597-019-0076-8.

Jung, M., Reichstein, M., Ciais, P., Seneviratne, S.I., Sheffield, J., Goulden, M.L., Bonan, G., Cescatti, A., Chen, J., de Jeu, R., Dolman, A.J., Eugster, W., Gerten, D., Gianelle, D., Gobron, N., Heinke, J., Kimball, J., Law, B.E., Montagnani, L., Mu, Q., Mueller, B., Oleson, K., Papale, D., Richardson, A.D., Roupsard, O., Running, S., Tomelleri, E., Viovy, N., Weber, U., Williams, C., Wood, E., Zaehle, S., Zhang, K., 2010. Recent decline in the global land evapotranspiration trend due to limited moisture supply. Nature 467, 951–954. http://dx.doi.org/10.1038/nature09396.

Kato, S., Rose, F.G., Rutan, D.A., Thorsen, T.J., Loeb, N.G., Doelling, D.R., Huang, X., Smith, W.L., Su, W., Ham, S.-H., 2018. Surface irradiances of edition 4.0 clouds and the Earth's radiant energy system (CERES) energy balanced and filled (EBAF) data product. J. Clim. 31, 4501–4527. http://dx.doi.org/10.1175/JCLI-D-17-0523.1.

L'Ecuyer, T.S., Beaudoing, H.K., Rodell, M., Olson, W., Lin, B., Kato, S., Clayson, C.A., Wood, E., Sheffield, J., Adler, R., Huffman, G., Bosilovich, M., Gu, G., Robertson, F., Houser, P.R., Chambers, D., Famiglietti, J.S., Fetzer, E., Liu, W.T., Gao, X., Schlosser, C.A., Clark, E., Lettenmaier, D.P., Hilburn, K., 2015. The observed state of the energy budget in the early twenty-first century. J. Clim. 28, 8319–8346. http://dx.doi.org/10.1175/JCLI-D-14-00556.1.

Liang, S., Cheng, J., Jia, K., Jiang, B., Liu, Q., Xiao, Z., Yao, Y., Yuan, W., Zhang, X., Zhao, X., Zhou, J., 2021. The global land surface satellite (GLASS) product suite. Bull. Am. Meteorol. Soc. 102, E323–E337. http://dx.doi.org/10.1175/BAMS-D-18-0341.1.

Liu, Y.Y., van Dijk, A.I.J.M., de Jeu, R.A.M., Canadell, J.G., McCabe, M.F., Evans, J.P., Wang, G., 2015. Recent reversal in loss of global terrestrial biomass. Nature Clim. Change 5, 470–474. http://dx.doi.org/10.1038/nclimate2581.

Liu, Y.Y., de Jeu, R.A.M., McCabe, M.F., Evans, J.P., van Dijk, A.I.J.M., 2011. Global long-term passive microwave satellite-based retrievals of vegetation optical depth. Geophys. Res. Lett. 38, http://dx.doi.org/10.1029/2011GL048684, URL http://onlinelibrary.wiley.com/doi/10.1029/2011GL048684.

Lundquist, J.D., Hughes, M., Henn, B., Gutmann, E.D., Livneh, B., Dozier, J., Neiman, P., 2015. High-elevation precipitation patterns: Using snow measurements to assess daily gridded datasets across the sierra nevada, California. J. Hydrometeorol. 16, 1773–1792. http://dx.doi.org/10.1175/JHM-D-15-0019.1.

Ma, N., Szilagyi, J., Zhang, Y., 2021. Calibration-free complementary relationship estimates terrestrial evapotranspiration globally. Water Resour. Res. 57, http://dx.doi.org/10.1029/2021WR029691, e2021WR029691.

Ma, N., Szilagyi, J., Zhang, Y., Liu, W., 2019. Complementary-relationship-based modeling of terrestrial evapotranspiration across China during 1982–2012: Validations and spatiotemporal analyses. J. Geophys. Res.: Atmos. 124, 4326–4351. http://dx.doi.org/10.1029/2018JD029850.

Ma, N., Zhang, Y., 2022. Increasing tibetan plateau terrestrial evapotranspiration primarily driven by precipitation. Agricult. Forest Meteorol. 317, 108887. http://dx.doi.org/10.1016/j.agrformet.2022.108887.

Maeght, J.-L., Rewald, B., Pierret, A., 2013. How to study deep roots—and why it matters. Front. Plant Sci. 4, http://dx.doi.org/10.3389/fpls.2013.00299, URL https://www.frontiersin.org/article/10.3389/fpls.2013.00299.

Martens, B., Miralles, D.G., Lievens, H., van der Schalie, R., de Jeu, R.A.M., Fernández-Prieto, D., Beck, H.E., Dorigo, W.A., Verhoest, N.E.C., 2017. GLEAM v3: Satellite-based land evaporation and root-zone soil moisture. Geosci. Model Dev. 10, 1903–1925. http://dx.doi.org/10.5194/gmd-10-1903-2017.

Miralles, D.G., De Jeu, R.A.M., Gash, J.H., Holmes, T.R.H., Dolman, A.J., 2011. Magnitude and variability of land evaporation and its components at the global scale. Hydrol. Earth Syst. Sci. 15, 967–981. http://dx.doi.org/10.5194/hess-15-967-2011.

Miralles, D.G., Gentine, P., Seneviratne, S.I., Teuling, A.J., 2019. Land-atmospheric feedbacks during droughts and heatwaves: State of the science and current challenges. Ann. New York Acad. Sci. 1436, 19–35. http://dx.doi.org/10.1111/nyas.13912.

Moesinger, L., Dorigo, W., de Jeu, R., van der Schalie, R., Scanlon, T., Teubner, I., Forkel, M., 2020. The global long-term microwave vegetation optical depth climate archive (VODCA). Earth Syst. Sci. Data 12, 177–196. http://dx.doi.org/10.5194/essd-12-177-2020.

Mu, Q., Zhao, M., Running, S.W., 2011. Improvements to a MODIS global terrestrial evapotranspiration algorithm. Remote Sens. Environ. 115, 1781–1800. http://dx.doi.org/10.1016/j.rse.2011.02.019.

Muñoz-Sabater, J., Dutra, E., Agustí Panareda, A., Albergel, C., Arduini, G., Balsamo, G., Boussetta, S., Choulga, M., Harrigan, S., Hersbach, H., Martens, B., Miralles, D.G., Piles, M., Rodríguez-Fernández, N.J., Zsoter, E., Buontempo, C., Thépaut, J.-N.l., 2021. ERA5-Land: A state-of-the-art global reanalysis dataset for land applications. Earth Syst. Sci. Data 13, 4349–4383. http://dx.doi.org/10.5194/essd-13-4349-2021.

Niu, G.-Y., Yang, Z.-L., 2006. Effects of frozen soil on snowmelt runoff and soil water storage at a continental scale. J. Hydrometeorol. 7, 937–952. http://dx.doi.org/10.1175/JHM538.1.

Oki, T., Kanae, S., 2006. Global hydrological cycles and world water resources. Science 313, 1068. http://dx.doi.org/10.1126/science.1128845.

Owe, M., Jeu, d.R., Holmes, T., 2008. Multisensor historical climatology of satellite-derived global land surface moisture. J. Geophys. Res. Earth Surf. 113, http://dx.doi.org/10.1029/2007JF000769, URL https://agupubs.onlinelibrary.wiley.com/doi/abs/10.1029/2007JF000769.

Pan, S., Pan, N., Tian, H., Friedlingstein, P., Sitch, S., Shi, H., Arora, V.K., Haverd, V., Jain, A.K., Kato, E., Lienert, S., Lombardozzi, D., Nabel, J.E.M.S., Ottlé, C., Poulter, B., Zaehle, S., Running, S.W. 2020. Evaluation of global terrestrial evapotranspiration using state-of-the-art approaches in remote sensing, machine learning and land surface modeling. Hydrol. Earth Syst. Sci. 24, 1485–1509. http://dx.doi.org/10.5194/hess-24-1485-2020.

Pastorello, G., Trotta, C., Canfora, E., Chu, H., Christianson, D., Cheah, Y.-W., Poindexter, C., Chen, J., Elbashandy, A., Humphrey, M., Isaac, P., Polidori, D., Reichstein, M., Ribeca, A., van Ingen, C., Vuichard, N., Zhang, L., Amiro, B., Ammann, C., Arain, M.A., Ardö, J., Arkebauer, T., Arndt, S.K., Arriga, N., Aubinet, M., Aurela, M., Baldocchi, D., Barr, A., Beamesderfer, E., Marchesini, L.B., Bergeron, O., Beringer, J., Bernhofer, C., Berveiller, D., Billesbach, D., Black, T.A., Blanken, P.D., Bohrer, G., Boike, J., Bolstad, P.V., Bonal, D., Bonnefond, J.-M., Bowling, D.R., Bracho, R., Brodeur, J., Brümmer, C., Buchmann, N., Burban, B., Burns, S.P., Buysse, P., Cale, P., Cavagna, M., Cellier, P., Chen, S., Chini, I., Christensen, T.R., Cleverly, J., Collalti, A., Consalvo, C., Cook, B.D., Cook, D., Coursolle, C., Cremonese, E., Curtis, P.S., D'Andrea, E., da Rocha, H., Dai, X., Davis, K.J., Cinti, B.D., Grandcourt, d.A., Ligne, A.D., De Oliveira, R.C., Delpierre, N., Desai, A.R., Di Bella, C.M., Tommasi, d.P., Dolman, H., Domingo, F., Dong, G., Dore, S., Duce, P., Dufrêne, E., Dunn, A., Dušek, D., Eichelmann, U., ElKhidir, H.A.M., Eugster, W., Ewenz, C.M., Ewers, B., Famulari, D., Fares, S., Feigenwinter, I., Feitz, A., Fensholt, R., Filippa, G., Fischer, M., Frank, J., Galvagno, M., Gharun, M., Gianelle, D., Gielen, B., Gioli, B., Gitelson, A., Goded, I., Goeckede, M., Goldstein, A.H., Gough, C.M., Goulden, M.L., Graf, A., Griebel, A., Gruening, C., Grünwald, T., Hammerle, A., Han, S., Han, X., Hansen, B.U., Hanson, C., Hatakka, J., He, Y., Hehn, M., Heinesch, B., Hinko-Najera, N., Hörtnagl, L., Hutley, L., Ibrom, A., Ikawa, H., Jackowicz-Korczynski, M., Janouš, D., Jans, W., Jassal, R., Jiang, S., Kato, T., Khomik, M., Klatt, J., Knohl, A., Knox, S., Kobayashi, H., Koerber, G., Kolle, O., Kosugi, Y., Kotani, A., Kowalski, A., Kruijt, B., Kurbatova, J., Kutsch, W.L., Kwon, H., Launiainen, S., Laurila, T., Law, B., Leuning, R., Li, Y., Liddell, M., Limousin, J.-M., Lion, M., Liska, J., Lohila, A., López-Ballesteros, A., López-Blanco, E., Loubet, B., Loustau, D., Lucas-Moffat, A., Lüers, J., Ma, S., Macfarlane, C., Magliulo, V., Maier, R., Mammarella, I., Manca, G., Marcolla, B., Margolis, H.A., Marras, S., Massman, W., Mastepanov, M., Matamala, R., Matthes, J.H., Mazzenga, F., McCaughey, H., McHugh, I., McMillan, A.M.S., Merbold, L., Meyer, W., Meyers, T., Miller, S.D., Minerbi, S., Moderow, U., Monson, R.K., Montagnani, L., Moore, C.E., Moors, E., Moreaux, V., Moureaux, C., Munger, J.W., Nakai, T., Neirynck, J., Nesic, Z., Nicolini, G., Noormets, A., Northwood, M., Nosetto, M., Nouvellon, Y., Novick, K., Oechel, W., Olesen, J.E., Ourcival, J.-M., Papuga, S.A., Parmentier, F.-J., Paul-Limoges, E., Pavelka, M., Peichl, M., Pendall, E., Phillips, R.P., Pilegaard, K., Pirk, N., Posse, G., Powell, T., Prasse, H., Prober, S.M., Rambal, S., Rannik, U., Raz-Yaseef, N., Rebmann, C., Reed, D., Dios, d.V.R., Restrepo-Coupe, N., Reverter, B.R., Roland, M., Sabbatini, S., Sachs, T., Saleska, S.R., Sánchez-Cañete, E.P., Sanchez-Mejia, Z.M., Schmid, H.P., Schmidt, M., Schneider, K., Schrader, F., Schroder, I., Scott, R.L., Sedlák, P., Serrano-Ortíz, P., Shao, C., Shi, P., Shironya, I., Siebicke, L., Šigut, L., Silberstein, R., Sirca, C., Spano, D., Steinbrecher, R., Stevens, R.M., Sturtevant, C., Suyker, A., Tagesson, T., Takanashi, S., Tang, Y., Tapper, N., Thom, J., Tomassucci, M., Tuovinen, J.-P., Urbanski, S., Valentini, R., van der Molen, M., van Gorsel, E., van Huissteden, K., Varlagin, A., Verfaillie, J., Vesala, T., Vincke, C., Vitale, D., Vygodskaya, N., Walker, J.P., Walter-Shea, E., Wang, H., Weber, R., Westermann, S., Wille, C., Wofsy, S., Wohlfahrt, G., Wolf, S., Woodgate, W., Li, Y., Zampedri, R., Zhang, J., Zhou, G., Zona, D., Agarwal, D., Biraud, S., Torn, M., Papale, D., 2020. The FLUXNET2015 dataset and the ONEFlux processing pipeline for Eddy covariance data. Sci. Data 7, 225. http://dx.doi.org/10.1038/s41597-020-0534-3.

Purdy, A.J., Fisher, J.B., Goulden, M.L., Colliander, A., Halverson, G., Tu, K., Famiglietti, J.S., 2018. SMAP soil moisture improves global evapotranspiration. Remote Sens. Environ. 219, 1–14. http://dx.doi.org/10.1016/j.rse.2018.09.023.

Rodell, M., Houser, P.R., Jambor, U., Gottschalck, J., Mitchell, K., Meng, C.-J., Arsenault, K., Cosgrove, B., Radakovich, J., Bosilovich, M., Entin, J.K., Walker, J.P., Lohmann, D., Toll, D., 2004. The global land data assimilation system. Bull. Am. Meteorol. Soc. 85, 381–394. http://dx.doi.org/10.1175/BAMS-85-3-381.

Scanlon, T.M., Kustas, W.P., 2012. Partitioning evapotranspiration using an Eddy covariance-based technique: Improved assessment of soil moisture and land–atmosphere exchange dynamics. Vadose Zone J. 11, http://dx.doi.org/10.2136/vzj2012.0025, vzj2012.0025.

Schneider, U., Becker, A., Finger, P., Meyer-Christoffer, A., Ziese, M., 2018. GPCC full data monthly product version 2018 at 0.5 degree: Monthly land-surface precipitation from rain-gauges built on GTS-based and historical data. Glob. Precip. Climatol. Centre http://dx.doi.org/10.5676/DWD_GPCC/FD_M_V2018_025.

Schwingshackl, C., Hirschi, M., Seneviratne, S.I., 2017. Quantifying spatiotemporal variations of soil moisture control on surface energy balance and near-surface air temperature. J. Clim. 30, 7105–7124. http://dx.doi.org/10.1175/JCLI-D-16-0727.1.

Siebert, S., Döll, P., 2010. Quantifying blue and green virtual water contents in global crop production as well as potential production losses without irrigation. Green-Blue Water Initiat., J. Hydrol. Green-Blue Water Initiat., vol. 384, 198–217.http://dx.doi.org/10.1016/j.jhydrol.2009.07.031,

Sulla-Menashe, D., Gray, J.M., Abercrombie, S.P., Friedl, M.A., 2019. Hierarchical mapping of annual global land cover 2001 to present: The MODIS collection 6 land cover product. Remote Sens. Environ. 222, 183–194. http://dx.doi.org/10.1016/j.rse.2018.12.013.

Ter Braak, C.J.F., Vrugt, J.A., 2008. Differential evolution Markov chain with snooker updater and fewer chains. Stat. Comput. 18, 435–446. http://dx.doi.org/10.1007/s11222-008-9104-9.

Teuling, A.J., Seneviratne, S.I., Stöckli, R., Reichstein, M., Moors, E., Ciais, P., Luyssaert, S., van den Hurk, B., Ammann, C., Bernhofer, C., Dellwik, E., Gianelle, D., Gielen, B., Grünwald, T., Klumpp, K., Montagnani, L., Moureaux, C., Sottocornola, M., Wohlfahrt, G., 2010. Contrasting response of European forest and grassland energy exchange to heatwaves. Nat. Geosci. 3, 722–727. http://dx.doi.org/10.1038/ngeo950.

Trenberth, K.E., Fasullo, J.T., Kiehl, J., 2009. Earth's global energy budget. Bull. Am. Meteorol. Soc. 90, 311–324. http://dx.doi.org/10.1175/2008BAMS2634.1.

Wang, K., Dickinson, R.E., 2012. A review of global terrestrial evapotranspiration: Observation, modeling, climatology, and climatic variability. Rev. Geophys. 50, http://dx.doi.org/10.1029/2011RG000373.

Wang, Y., Zhou, J., Ma, R., Zhu, G., Zhang, Y., 2022. Development of a new pedotransfer function addressing limitations in soil hydraulic models and observations. Water Resour. Res. 58, http://dx.doi.org/10.1029/2021WR031406, e2021WR031406.

Wieder, W.R., Boehnert, J., Bonan, G.B., Langseth, M., 2014. Regridded harmonized world soil database v1. 2. ORNL DAAC.

Wiese, D.N., Landerer, F.W., Watkins, M.M., 2016. Quantifying and reducing leakage errors in the JPL RL05M GRACE mascon solution. Water Resour. Res. 52, 7490–7502. http://dx.doi.org/10.1002/2016WR019344.

Wild, M., Folini, D., Hakuba, M.Z., Schär, C., Seneviratne, S.I., Kato, S., Rutan, D., Ammann, C., Wood, E.F., König-Langlo, G., 2015. The energy balance over land and oceans: An assessment based on direct observations and CMIP5 climate models. Clim. Dynam. 44, 3393–3429. http://dx.doi.org/10.1007/s00382-014-2430-z.

Xiong, W., Tang, G., Wang, T., Ma, Z., Wan, W., 2022. Evaluation of IMERG and ERA5 precipitation-phase partitioning on the global scale. Water 14, 1122. http://dx.doi.org/10.3390/w14071122.

Xu, Z., Chen, X., Liu, J., Zhang, Y., Chau, S., Bhattarai, N., Wang, Y., Li, Y., Connor, T., Li, Y., 2020. Impacts of irrigated agriculture on food–energy–water–CO2 nexus across metacoupled systems. Nature Commun. 11, 5837. http://dx.doi.org/10.1038/s41467-020-19520-3.

Zeng, Z., Wang, T., Zhou, F., Ciais, P., Mao, J., Shi, X., Piao, S., 2014. A worldwide analysis of spatiotemporal changes in water balance-based evapotranspiration from 1982 to 2009. J. Geophys. Res.: Atmos. 119, 1186–1202. http://dx.doi.org/10.1002/2013JD020941.

Zhang, K., Kimball, J.S., Nemani, R.R., Running, S.W., Hong, Y., Gourley, J.J., Yu, Z., 2015. Vegetation greening and climate change promote multidecadal rises of global land evapotranspiration. Sci. Rep. 5, 75–77. http://dx.doi.org/10.1038/srep15956.

Zhang, Y., Kong, D., Gan, R., Chiew, F.H.S., McVicar, T.R., Zhang, Q., Yang, Y., 2019a. Coupled estimation of 500 m and 8-day resolution global evapotranspiration and gross primary production in 2002–2017. Remote Sens. Environ. 222, 165–182. http://dx.doi.org/10.1016/j.rse.2018.12.031.

Zhang, K., Li, X., Zheng, D., Zhang, L., Zhu, G., 2022. Estimation of global irrigation water use by the integration of multiple satellite observations. Water Resour. Res. 58, http://dx.doi.org/10.1029/2021WR030031, e2021WR030031.

Zhang, K., Ma, J., Zhu, G., Ma, T., Han, T., Feng, L.L., 2017. Parameter sensitivity analysis and optimization for a satellite-based evapotranspiration model across multiple sites using moderate resolution imaging spectroradiometer and flux data. J. Geophys. Res.: Atmos. 122, 230–245. http://dx.doi.org/10.1002/2016JD025768.

Zhang, Y., Peña-Arancibia, J.L., McVicar, T.R., Chiew, F.H.S., Vaze, J., Liu, C., Lu, X., Zheng, H., Wang, Y., Liu, Y.Y., Miralles, D.G., Pan, M., 2016. Multi-decadal trends in global terrestrial evapotranspiration and its components. Sci. Rep. 6, http://dx.doi.org/10.1038/srep19124.

Zhang, K., Zhu, G., Ma, J., Yang, Y., Shang, S., Gu, C., 2019b. Parameter analysis and estimates for the MODIS evapotranspiration algorithm and multiscale verification. Water Resour. Res. 55, 2211–2231. http://dx.doi.org/10.1029/2018WR023485.

Zhou, S., Williams, A.P., Lintner, B.R., Berg, A.M., Zhang, Y., Keenan, T.F., Cook, B.I., Hagemann, S., Seneviratne, S.I., Gentine, P., 2021. Soil moisture–atmosphere feedbacks mitigate declining water availability in drylands. Nature Clim. Change 11, 38–44. http://dx.doi.org/10.1038/s41558-020-00945-z.

Zhu, G., Li, X., Zhang, K., Ding, Z., Han, T., Ma, J., Huang, C., He, J., Ma, T., 2016. Multi-model ensemble prediction of terrestrial evapotranspiration across north China using Bayesian model averaging. Hydrol. Process. 30, 2861–2879. http://dx.doi.org/10.1002/hyp.10832.

Zhu, G., Zhang, K., Chen, H., Wang, Y., Su, Y., Zhang, Y., Ma, J., 2019. Development and evaluation of a simple hydrologically based model for terrestrial evapotranspiration simulations. J. Hydrol. 577, 123928. http://dx.doi.org/10.1016/j.jhydrol.2019.123928.